



# A mass-weighted isentropic coordinate for mapping chemical tracers and computing atmospheric inventories

Yuming Jin<sup>1</sup>, Ralph F. Keeling<sup>1</sup>, Eric J. Morgan<sup>1</sup>, Eric Ray<sup>2</sup>, Nicholas C. Parazoo<sup>3</sup>, and Britton B. Stephens<sup>4</sup>

<sup>1</sup>Scripps Institution of Oceanography, University of California San Diego, La Jolla, CA 92093, USA

<sup>2</sup>National Oceanic and Atmospheric Administration, Boulder, CO 80305, USA

<sup>3</sup>Jet Propulsion Laboratory, California Institute of Technology, Pasadena, CA 91109, USA

<sup>4</sup>National Center for Atmospheric Research, Boulder, CO 80301, USA

**Correspondence:** Yuming Jin (y2jin@ucsd.edu)

Received: 13 August 2020 – Discussion started: 19 August 2020

Revised: 5 November 2020 – Accepted: 24 November 2020 – Published: 12 January 2021

**Abstract.** We introduce a transformed isentropic coordinate  $M_{\theta_e}$ , defined as the dry air mass under a given equivalent potential temperature surface ( $\theta_e$ ) within a hemisphere. Like  $\theta_e$ , the coordinate  $M_{\theta_e}$  follows the synoptic distortions of the atmosphere but, unlike  $\theta_e$ , has a nearly fixed relationship with latitude and altitude over the seasonal cycle. Calculation of  $M_{\theta_e}$  is straightforward from meteorological fields. Using observations from the recent HIPPO and Atmospheric Tomography Mission (ATom) airborne campaigns, we map the CO<sub>2</sub> seasonal cycle as a function of pressure and  $M_{\theta_e}$ , where  $M_{\theta_e}$  is thereby effectively used as an alternative to latitude. We show that the CO<sub>2</sub> seasonal cycles are more constant as a function of pressure using  $M_{\theta_e}$  as the horizontal coordinate compared to latitude. Furthermore, short-term variability in CO<sub>2</sub> relative to the mean seasonal cycle is also smaller when the data are organized by  $M_{\theta_e}$  and pressure than when organized by latitude and pressure. We also present a method using  $M_{\theta_e}$  to compute mass-weighted averages of CO<sub>2</sub> on a hemispheric scale. Using this method with the same airborne data and applying corrections for limited coverage, we resolve the average CO<sub>2</sub> seasonal cycle in the Northern Hemisphere (mass-weighted tropospheric climatological average for 2009–2018), yielding an amplitude of  $7.8 \pm 0.14$  ppm and a downward zero-crossing on Julian day  $173 \pm 6.1$  (i.e., late June).  $M_{\theta_e}$  may be similarly useful for mapping the distribution and computing inventories of any long-lived chemical tracer.

## 1 Introduction

The spatial and temporal distribution of long-lived chemical tracers like CO<sub>2</sub>, CH<sub>4</sub>, and O<sub>2</sub> / N<sub>2</sub> typically includes regular seasonal cycles and gradients with latitude and pressure (Conway and Tans, 1999; Ehhalt, 1978; Randerson et al., 1997; Rasmussen and Khalil, 1981; Tohjima et al., 2012). These patterns are evident in climatological averages but are potentially distorted on short timescales by synoptic weather disturbances, especially at middle to high latitudes (i.e., poleward of 30° N and S) (Parazoo et al., 2008; Wang et al., 2007). With a temporally dense dataset such as from satellite remote sensing or tower in situ measurements, climatological averages can be created by averaging over this variability. For temporally sparse datasets such as from airborne campaigns, it may be necessary to correct for synoptic distortion.

A common approach to correct synoptic distortion is to use transformed coordinates rather than geographic coordinates (i.e., pressure–latitude), to take into account atmospheric dynamics and transport barriers. Such coordinate transformation has been used, for example, to reduce dynamically induced variability in the stratosphere using equivalent latitude rather than latitude as the horizontal coordinate (Butchart and Remsberg, 1986); to diagnose the tropopause profile using a tropopause-based rather than surface-based vertical coordinate (Birner et al., 2002); to study the transport regime in the Arctic using a horizontal coordinate based on the polar dome (Bozem et al., 2019); and to study UTLS (upper troposphere–lower stratosphere) tracer data by using tropopause-based, jet-based, and equivalent latitude coordi-

nates (Petropavlovskikh et al., 2019). In the troposphere, a transformed coordinate, the isentropic coordinate ( $\theta$ ), has been widely applied to evaluate the distribution of tracer data (Miyazaki et al., 2008; Parazoo et al., 2011, 2012). As air parcels move with synoptic disturbances,  $\theta$  and the tracer tend to be similarly displaced so that the  $\theta$ –tracer relationship is relatively conserved (Keppel-Aleks et al., 2011). Furthermore, vertical mixing tends to be rapid on  $\theta$  surfaces, so  $\theta$  and tracer contours are often nearly parallel (Barnes et al., 2016). However,  $\theta$  varies greatly with latitude and altitude over seasons due to changes in heating and cooling with solar insolation, which complicates the interpretation of  $\theta$ –tracer relationships on seasonal timescales.

During analysis of airborne data from the HIAPER Pole-to-Pole Observations (HIPPO) (Wofsy, 2011) and the Atmospheric Tomography Mission (ATom) (Prather et al., 2018) airborne campaigns, we have found it useful to transform potential temperature into a mass-based unit,  $M_\theta$ , which we define as the total mass of dry air under a given isentropic surface in the hemisphere. In contrast to  $\theta$ , which has large seasonal variation,  $M_\theta$  has a more stable relationship to latitude and altitude, while varying in parallel with  $\theta$  on synoptic scales. Also, for a tracer which is well-mixed on  $\theta$ , a plot of this tracer versus  $M_\theta$  can be directly integrated to yield the atmospheric inventory of the tracer, because  $M_\theta$  directly corresponds to the mass of air. We note that a similar concept to  $M_{\theta_e}$  has been introduced in the stratosphere by Linz et al. (2016), in which  $M(\theta)$  is defined as the mass above the  $\theta$  surface, to study the relationship between age of air and diabatic circulation of the stratosphere.

Several choices need to be made in the definition of  $M_\theta$ , including defining boundary conditions (e.g., in altitude and latitude) for mass integration and whether to use potential temperature  $\theta$  or equivalent potential temperature  $\theta_e$ . Here, for boundaries, we use the dynamical tropopause (based on the potential vorticity unit, PVU) and the Equator, thus integrating the dry air mass of the troposphere in each hemisphere. We also focus on  $M_\theta$  defined using equivalent potential temperature ( $\theta_e$ ) to conserve moist static energy in the presence of latent heating during vertical motion, which improves alignment between mass transport and mixing especially within storm tracks in mid-latitudes (Parazoo et al., 2011; Pauluis et al., 2008, 2010). We call this tracer  $M_{\theta_e}$ .

In this paper we describe the method for calculating  $M_{\theta_e}$  and discuss its variability on synoptic to seasonal scales. We also discuss the time variation in the  $\theta_e$ – $M_{\theta_e}$  relationship within each hemisphere and explore the stability of  $M_{\theta_e}$  and the  $\theta_e$ – $M_{\theta_e}$  relationship using different reanalysis products. To illustrate the application of  $M_{\theta_e}$ , we map CO<sub>2</sub> data from two recent airborne campaigns (HIPPO and ATom) on  $M_{\theta_e}$ . Further, we show how  $M_{\theta_e}$  can be used to accurately compute the average CO<sub>2</sub> concentration over the entire troposphere of the Northern Hemisphere using measurements from the same airborne campaigns. We examine the accuracy of this method and propose an appropriate way to sample the atmo-

sphere with aircraft to compute the average of a chemical tracer within a large zonal domain.

## 2 Methods

### 2.1 Meteorological reanalysis products

The calculation of  $M_{\theta_e}$  requires the distribution of dry air mass and  $\theta_e$ . For these quantities, we alternately use three reanalysis products: ERA-Interim (Dee et al., 2011), NCEP2 (Kanamitsu et al., 2002), and Modern-Era Retrospective analysis for Research and Applications Version 2 (MERRA-2) (Gelaro et al., 2017). All products have a 2.5° horizontal resolution. NCEP2 has a daily resolution, and we average 6-hourly ERA-Interim fields and 3-hourly MERRA-2 fields to yield daily fields. ERA-Interim has 32 vertical levels from 1000 to 1 mbar, with approximately 20 to 27 levels in the troposphere. NCEP2 has 17 vertical levels from 1000 to 10 mbar, with approximately 8 to 12 levels in the troposphere. MERRA-2 has 42 vertical levels from 985 to 0.01 mbar, with approximately 21 to 25 levels in the troposphere.

### 2.2 Equivalent potential temperature ( $\theta_e$ ) and dry air mass (M) of the atmospheric fields

We compute  $\theta_e$  (K) using the following expression:

$$\theta_e = \left( T + \frac{L_v(T)}{C_{pd}} \cdot w \right) \cdot \left( \frac{P_0}{P} \right)^{\frac{R_d}{C_{pd}}} \quad (1)$$

from Stull (2012).  $T$  (K) is the temperature of air;  $w$  (kg of water vapor per kg of air mass) is the water vapor mixing ratio;  $R_d$  (287.04 J kg<sup>-1</sup> K<sup>-1</sup>) is the gas constant for air;  $C_{pd}$  (1005.7 J kg<sup>-1</sup> K<sup>-1</sup>) is the specific heat of dry air at constant pressure;  $P_0$  (1013.25 mbar) is the reference pressure at the surface, and  $L_v(T)$  is the latent heat of evaporation at temperature  $T$ .  $L_v(T)$  is defined as 2406 kJ kg<sup>-1</sup> at 40 °C and 2501 kJ kg<sup>-1</sup> at 0 °C and scales linearly with temperature.

Following Bolton (1980), we compute the water vapor mixing ratio ( $w$ ) from relative humidity (RH; kg kg<sup>-1</sup>) provided by the reanalysis products and the formula for the saturation mixing ratio of water vapor ( $P_{s,v}$ ; mbar) modified by Wexler (1976).

$$P_{s,v} = 0.06122 \cdot e^{\frac{17.67 \cdot T}{T+243.5}} \quad (2)$$

$$w = \text{RH} \cdot 0.622 \cdot \frac{P_{s,v}}{P - P_{s,v}} \quad (3)$$

We compute the total air mass of each grid cell  $x$  at time  $t$ ,  $M_x(t)$ , shown in Eq. (4), from the product of the pressure range and surface area and divided by a latitude- and height-dependent gravity constant provided by Arora et al. (2011). The surface area is computed by using latitude ( $\Phi$ ), longitude

( $\lambda$ ), and the radius of the Earth ( $R$ , 6371 km). The total air mass of each grid cell is computed from

$$M_x = \frac{\Delta P}{g} \cdot |\Delta \sin(\Phi) \cdot \Delta \lambda| \cdot R^2, \quad (4)$$

where  $\Delta$  represents the difference between two boundaries of each grid cell.

The gravity constant ( $g$ ;  $\text{kg m}^{-2}$ ) is computed following Arora et al. (2011) as

$$g(\Phi, h) = g_0 \cdot \left( 1 + 0.0053 \cdot \sin^2(\Phi) - 0.000006 \cdot \sin^2(2 \cdot \Phi) \right) - 0.000003086 \cdot h, \quad (5)$$

where the reference gravity constant ( $g_0$ ) is assumed to be  $9.78046 \text{ m s}^{-2}$  and the height ( $h$ ) in units of meters is computed from

$$P = P_0 \cdot e^{-\frac{h}{H}}, \quad (6)$$

where  $H$  is the scale height of the atmosphere and assumed to be 8400 m.

The dry air mass is then computed by subtracting the water mass, computed from relative humidity, the saturation water vapor mass mixing ratio, and the total air mass of the grid cell (Eq. 3). Since this study focuses on tracer distributions in the troposphere, we compute  $M_{\theta_e}$  with an upper boundary at the dynamical tropopause defined as the 2 PVU (potential vorticity units,  $10^{-6} \text{ K kg}^{-1} \text{ m}^2 \text{ s}^{-1}$ ) surface.

ERA-Interim and NCEP2 include hypothetical levels below the true land or sea surface, for example, the 850 hPa level over the Himalaya, which we exclude in the calculation of  $M_{\theta_e}$ .

### 2.3 Determination of $M_{\theta_e}$

We show a schematic of the conceptual basis for the calculation of  $M_{\theta_e}$  in Fig. 1. To compute  $M_{\theta_e}$ , we sort all tropospheric grid cells in the hemisphere by increasing  $\theta_e$  and sum the dry air mass over grid cells following

$$M_{\theta_e}(\theta_e, t) = \sum M_x(t)|_{\theta_{e_x} < \theta_e}, \quad (7)$$

where  $M_x(t)$  is the dry air mass of each grid cell  $x$  at time  $t$  and  $\theta_{e_x}$  is the equivalent potential temperature of the grid cell. The sum is over all grid cells with  $\theta_{e_x}$  less than  $\theta_e$ .

This calculation yields a unique value of  $M_{\theta_e}$  for each value of  $\theta_e$ . We refer to the relationship between  $\theta_e$  and  $M_{\theta_e}$  as the “ $\theta_e$ – $M_{\theta_e}$  look-up table”, which we generate at daily resolution. We provide this look-up table for each hemisphere computed from ERA-Interim from 1980 to 2018 with a daily resolution and from the lowest to the highest  $\theta_e$  surface in the troposphere with 1 K intervals (see data availability).

## 3 Characteristics of $M_{\theta_e}$

### 3.1 Spatial and temporal distribution of $M_{\theta_e}$

Figure 2 shows snapshots of the distribution of zonal average  $\theta_e$  and  $M_{\theta_e}$  with latitude and pressure at two arbitrary time slices (1 January 2009, 1 July 2009).  $M_{\theta_e}$  is not continuous across the Equator because it is defined separately in each hemisphere. By definition, each  $M_{\theta_e}$  surface is exactly aligned with a corresponding  $\theta_e$  surface, and  $M_{\theta_e}$  surfaces have the same characteristics as  $\theta_e$  surfaces, which decrease with latitude and generally increase with altitude. Whereas the zonal average  $\theta_e$  surfaces vary by up to  $20^\circ$  in latitude over seasons, the meridional displacement of zonal average  $M_{\theta_e}$  is much smaller, with less than  $5^\circ$  in latitude poleward of  $30^\circ$  N and S, as expected, because the zonal average displacement of atmospheric mass over seasons is small. This small seasonal displacement is closely associated with the seasonality of vertical sloping of  $\theta_e$  surfaces (Fig. 2). As the mass under each  $M_{\theta_e}$  surface is always constant, the change in tilt must cause the meridional displacement. In the summer, the tilt is steeper (due to increased deep convection), so  $M_{\theta_e}$  surfaces move poleward in the lower troposphere but move equatorward in the upper troposphere.

$M_{\theta_e}$  surfaces at given meridians (Fig. 3) in the Northern Hemisphere show clear zonal asymmetry, with larger and more complex displacements compared to the zonal averages, associated with differential heating by land and ocean and orographic stationary Rossby waves (Hoskins and Karoly, 1981; Wills and Schneider, 2018). For example, over the Northern Hemisphere ocean at  $180^\circ$  E (Fig. 3a) and from the summer to winter,  $M_{\theta_e}$  surfaces move poleward in the middle to high latitudes (e.g., poleward of  $45^\circ$  N) but move equatorward in the mid- to low-latitude lower troposphere (e.g., equatorward of  $45^\circ$  N, 900–700 mbar), with the magnitude smaller than  $10^\circ$  latitude in both. In comparison, over the Northern Hemisphere land at  $100^\circ$  E (Fig. 3b) and from the summer to winter,  $M_{\theta_e}$  surfaces move equatorward by up to  $30^\circ$  latitude, except in the high-latitude middle troposphere (e.g., poleward of  $70^\circ$  N,  $\sim 500$  mbar), where the flat  $M_{\theta_e}$  surfaces lead to slightly poleward displacements. In the Southern Hemisphere, in contrast, the summer-to-winter displacements of the 180 and  $100^\circ$  E sections are similar to the zonal average.

At lower latitudes, the zonal averages of  $M_{\theta_e}$  and  $\theta_e$  both exhibit strong secondary maxima near the surface associated with the Hadley circulation (equatorward of  $30^\circ$  N and S) and in the summer, driven by high water vapor. From the contours in Fig. 2, this surface branch of high  $M_{\theta_e}$  and  $\theta_e$  appears disconnected from the upper tropospheric branch. In fact, these two branches are connected through air columns undergoing deep convection, which are not resolved in the zonal means shown in Fig. 2 but are resolved in some meridians (e.g., Fig. 3a). We also note that, over the land at  $100^\circ$  E (Fig. 3b), the two disconnected  $M_{\theta_e}$  and  $\theta_e$  branches in the

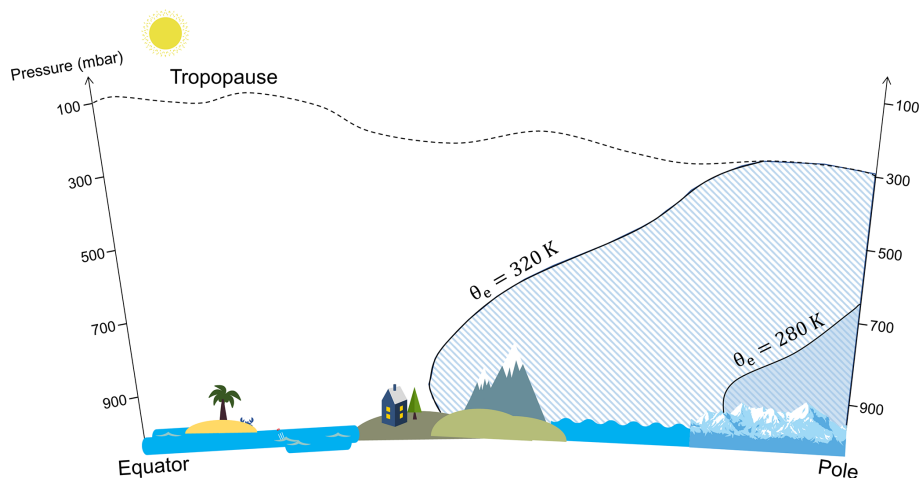


**Figure 1.** Schematic of the conceptual basis to calculate  $M_{\theta_e}$ .  $M_{\theta_e}$  of a given  $\theta_e$  surface is computed by summing all dry air mass with a low equivalent potential temperature in the troposphere of the hemisphere. This calculation yields a unique  $\theta_e$ – $M_{\theta_e}$  relation at a given time point.

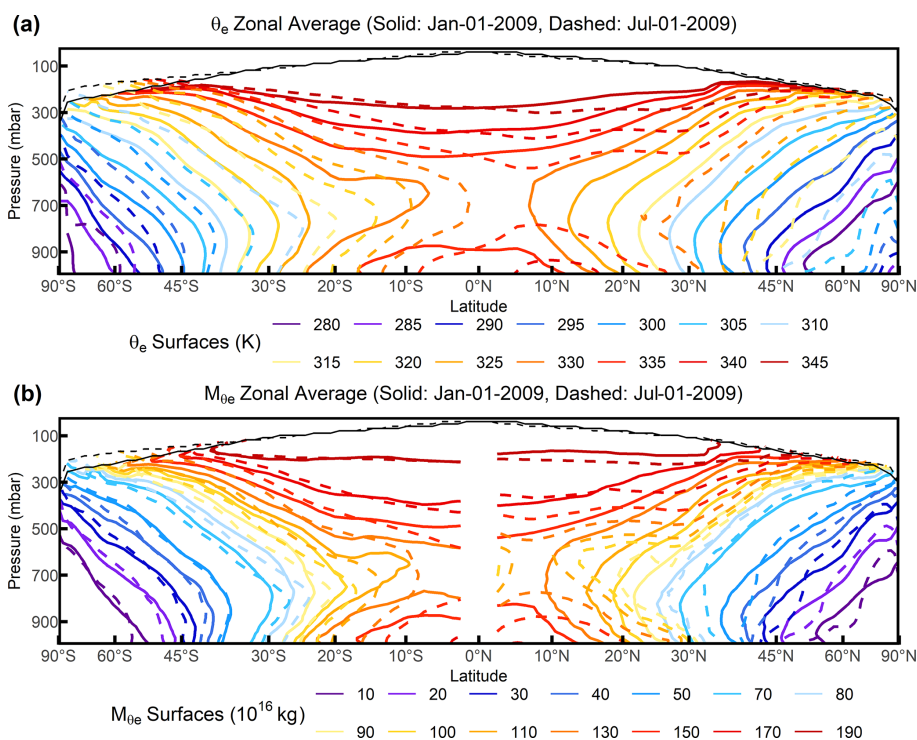
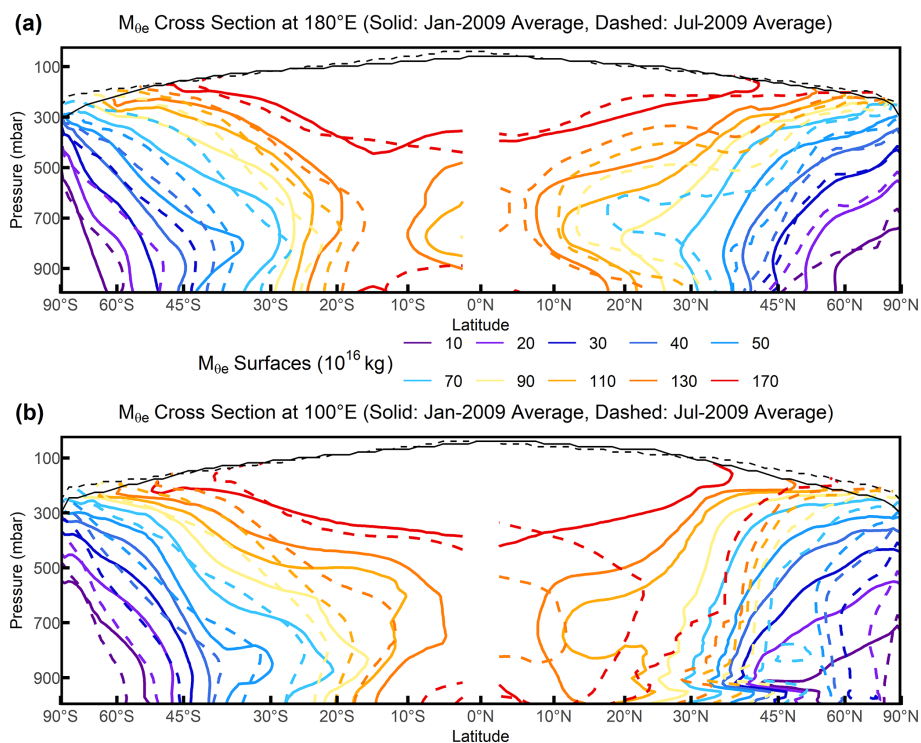


**Figure 2.** Snapshot of the distribution of (a) zonal average  $\theta_e$  surfaces on 1 January 2009 (solid lines) and 1 July 2009 (dashed lines) and (b) zonal average  $M_{\theta_e}$  surfaces on 1 January 2009 (solid lines) and 1 July 2009 (dashed lines). The zonal average tropopause is also shown here for 1 January 2009 (solid black line) and 1 July 2009 (dashed black line).  $\theta_e$ ,  $M_{\theta_e}$ , and the tropopause are computed from ERA-Interim.

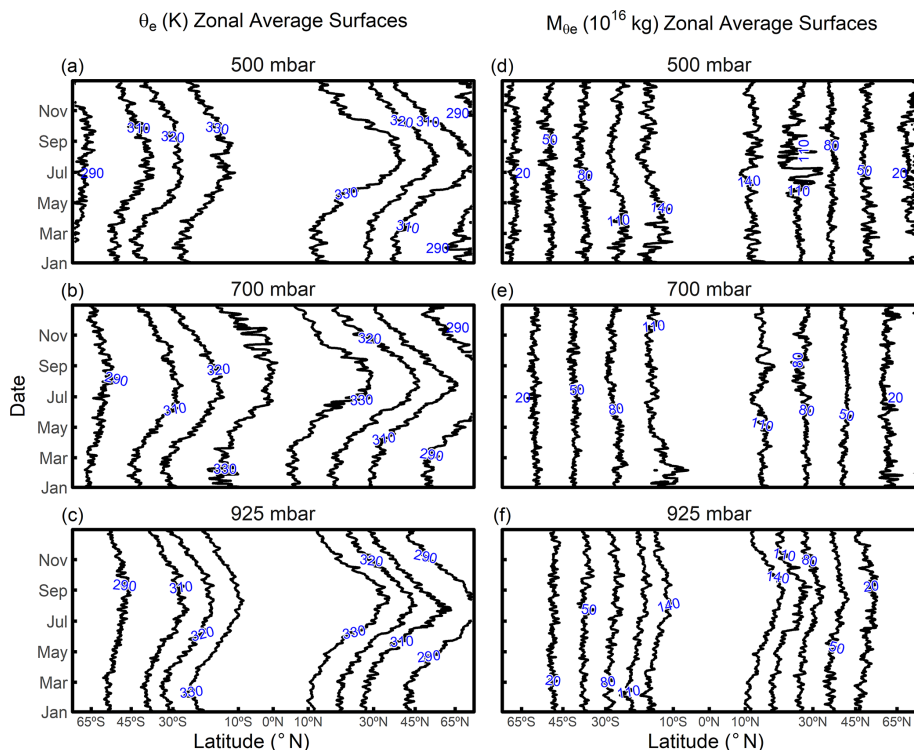
Northern Hemisphere summer are displaced poleward compared to the zonal average, consistent with a northward shift of the intertropical convergence zone (ITCZ) over southern Asia. The existence of these two branches may limit some applications of  $M_{\theta_e}$ , as discussed in Sect. 4.

Figure 4 shows the zonal average meridional displacement of  $\theta_e$  and  $M_{\theta_e}$  with a daily resolution. In summer,  $M_{\theta_e}$  sur-

faces displace poleward in the lower troposphere but equatorward in the upper troposphere. The displacements in the lower troposphere (925 mbar) are greater in the Northern Hemisphere, where the  $M_{\theta_e} = 140 \times 10^{16}$  kg surface, for example, displaces poleward by  $10^\circ$  in latitude between winter and summer (Fig. 4b). Besides the seasonal variability, Fig. 4 also shows evident synoptic-scale variability.



**Figure 3.**  $M_{\theta_e}$  surfaces as January 2009 average (solid lines) and July 2009 average (dashed lines) for (a) 180° E (mostly over the Pacific Ocean), and (b) 100° E (mostly over the Eurasia land in the Northern Hemisphere).  $M_{\theta_e}$  and the tropopause are computed from ERA-Interim.



**Figure 4.** Time series of meridional displacement of selected zonal average  $\theta_e$  (K) surfaces over a year at (a) 500 mbar, (b) 700 mbar, and (c) 925 mbar. Meridional displacement of selected zonal average  $M_{\theta_e}$  ( $10^{16}$  kg) surfaces over a year at (d) 500 mbar, (e) 700 mbar, and (f) 925 mbar. The value of each surface is labeled.  $\theta_e$  and  $M_{\theta_e}$  are computed from ERA-Interim. Results shown are for the year 2009.

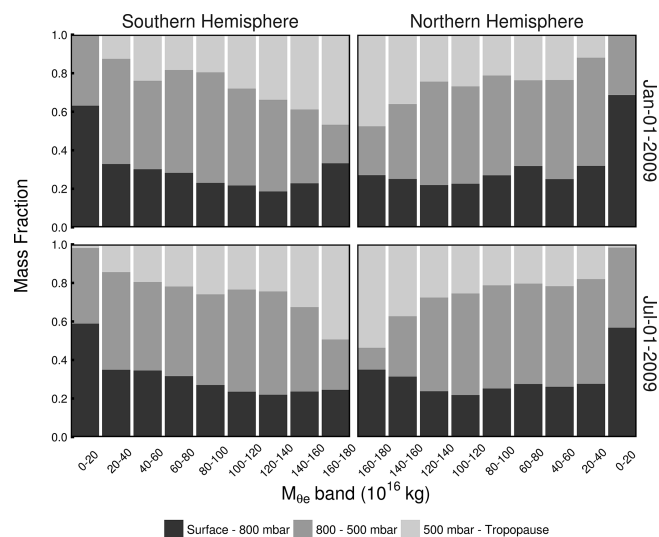


**Figure 5.** Snapshots (1 January 2009 and 1 July 2009) of the mass distribution of different  $M_{\theta_e}$  bins from three pressure bins (surface to 800 mbar, 800 to 500 mbar, and 500 mbar to tropopause).  $M_{\theta_e}$  is computed from ERA-Interim. Low  $M_{\theta_e}$  bins are seen to have larger contributions from the air near the surface, and high  $M_{\theta_e}$  bins have larger contributions from air aloft. Comparing the top and the bottom panels shows that the seasonal differences in pressure contributions are small except for the highest  $M_{\theta_e}$  bins ( $160 \times 10^{16}$ – $180 \times 10^{16}$  kg) and the lowest  $M_{\theta_e}$  bin in the Northern Hemisphere ( $0$ – $20 \times 10^{16}$  kg).

Since the tilting of  $\theta_e$  surfaces has an impact on the seasonal displacement of  $M_{\theta_e}$  surfaces, the contribution of different pressure levels to the mass of a given  $M_{\theta_e}$  bin must also vary with season. In Fig. 5, we show these contributions as two daily snapshots on 1 January and 1 July 2009. Low  $M_{\theta_e}$  bins consist of air masses mostly below 500 mbar near the pole. As  $M_{\theta_e}$  increases, the contribution from the upper troposphere gradually increases while the contribution from the surface to 800 mbar decreases to its minimum at around  $100 \times 10^{16}$  to  $120 \times 10^{16}$  kg. The contribution from the surface to 800 mbar increases as  $M_{\theta_e}$  increases above  $120 \times 10^{16}$  kg. The mass fraction shows only small variations with season, with the lower troposphere (surface to 800 mbar) contributing slightly less in the low- $M_{\theta_e}$  bands and slightly more in the high- $M_{\theta_e}$  bands in the summer, which is closely related to the seasonal tilting of corresponding  $\theta_e$  surfaces.

### 3.2 $\theta_e$ – $M_{\theta_e}$ relationship

Figure 6 compares the temporal variation in  $M_{\theta_e}$  of several given  $\theta_e$  surfaces (i.e.,  $\theta_e$ – $M_{\theta_e}$  look-up table) computed from different reanalysis products for 2009. The deviations are indistinguishable between ERA-Interim and MERRA-2, except near  $\theta_e = 340$  K, where MERRA-2 is systematically lower than ERA-Interim by  $1.5 \times 10^{16}$  to  $6.5 \times 10^{16}$  kg.

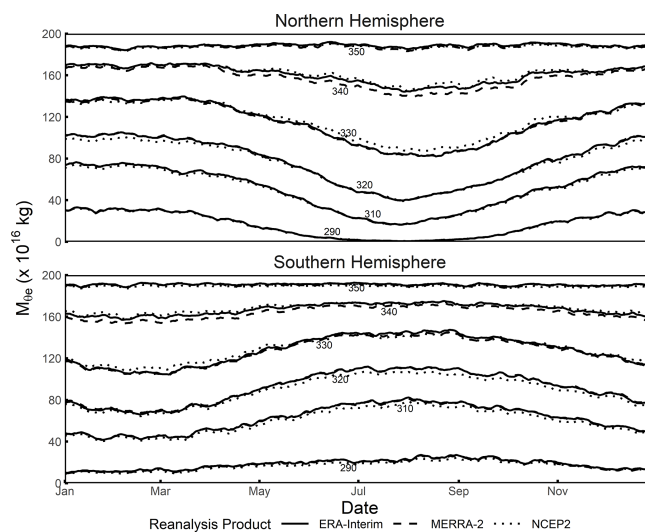


**Figure 6.** Variability in  $M_{\theta_e}$  of given  $\theta_e$  surfaces (i.e.,  $\theta_e$ – $M_{\theta_e}$  look-up table) over a year with a daily resolution in the Northern and Southern Hemisphere. Data from ERA-Interim are shown as a solid line; MERRA-2 data are shown as a dashed line, and NCEP2 data are shown as a dotted line. Results shown are for the year 2009.

NCEP2 shows slightly larger deviations from ERA-Interim but by less than  $8.5 \times 10^{16}$  kg. The products are highly consistent in seasonal variability, and they also show agreement on synoptic timescales. The small difference between products is expected because of different resolutions and methods (Mooney et al., 2011). We expect these differences would be negligible for most applications of  $M_{\theta_e}$ .

Figure 6 shows that, in both hemispheres,  $M_{\theta_e}$  reaches its minimum in summer and maximum in winter for a given  $\theta_e$  surface, with the largest seasonality at the lowest  $\theta_e$  (or  $M_{\theta_e}$ ) values. The seasonality decreases as  $\theta_e$  increases, following the reduction in the seasonality of shortwave absorption at lower latitudes (Li and Leighton, 1993). The seasonality is smaller in the Southern Hemisphere, consistent with the larger ocean area and hence greater heat capacity and transport (Fasullo and Trenberth, 2008; Foltz and McPhaden, 2006). Figure 6 also shows that  $M_{\theta_e}$  has significant synoptic-scale variability although smaller than the seasonal variability. Synoptic variability is typically larger in winter than summer, as discussed below.

### 3.3 Relationship to diabatic heating and mass fluxes

A key step of the application of  $M_{\theta_e}$  for interpreting tracer data is the generation of the look-up table that relates  $\theta_e$  and  $M_{\theta_e}$ . In this section, we address a tangential question of what controls the temporal variation in the look-up table, which is not necessary for the application but may be of fundamental meteorological interest.

As shown in Appendix A, the temporal variation in the look-up table,  $\dot{M}_{\theta_e} = \frac{\partial}{\partial t} M_{\theta_e}(\theta_e, t)$ , can be related to underly-

ing mass and heat fluxes according to

$$\dot{M}_{\theta_e} = -\frac{1}{C_{pd}} \frac{\partial Q_{dia}(\theta_e, t)}{\partial \theta_e} + m_T(\theta_e, t) + m_E(\theta_e, t), \quad (8)$$

where  $\frac{\partial Q_{dia}(\theta_e, t)}{\partial \theta_e}$  ( $J s^{-1} K^{-1}$ ) is the effective diabatic heating, integrated over the full  $\theta_e$  surface per unit width in  $\theta_e$ ;  $m_T(\theta_e, t)$  ( $kg s^{-1}$ ) is the net mass flux across the tropopause; and  $m_E(\theta_e, t)$  ( $kg s^{-1}$ ) is the net mass flux across the Equator, including all air with equivalent potential temperature of less than  $\theta_e$ .  $Q_{dia}$  has contributions from internal heating without ice formation ( $Q'_{int}$ ), heating from ice formation ( $Q_{ice}$ ), sensible heating from the surface ( $Q_{sen}$ ), surface evaporation ( $Q_{evap}$ ), turbulent diffusion of heat ( $Q_{diff}$ ), and turbulent transport of water vapor ( $Q_{H_2O}$ ) following

$$Q_{dia}(\theta_e, t) = Q'_{int}(\theta_e, t) + Q_{ice}(\theta_e, t) + Q_{sen}(\theta_e, t) + Q_{evap}(\theta_e, t) + Q_{diff}(\theta_e, t) + Q_{H_2O}(\theta_e, t). \quad (9)$$

The terms  $Q_{evap}$  and  $Q_{H_2O}$  are expressed as heating rates by multiplying the underlying water fluxes by  $L_v(T)/C_{pd}$ . In order to quantify the dominant processes contributing to temporal variation in  $M_{\theta_e}$ , the terms in Eqs. (8) and (9) must be linked to diagnostic variables available in the reanalysis or model products. Although there was no perfect match with any of the three reanalysis products, MERRA-2 provides temperature tendencies for individual processes, which can be converted to heating rates per Eq. 9 following

$$\frac{\partial Q_i(\theta_e, t)}{\partial \theta_e} = \frac{C_{pd}}{\Delta \theta_e} \sum_x \left( \frac{dT}{dt} \right)_{x,i} M_x, \quad (10)$$

where  $i$  refers to a specific process ( $Q'_{int}$ ,  $Q_{ice}$ , etc.),  $\left( \frac{dT}{dt} \right)_x$  ( $K s^{-1}$ ) is the temperature tendency of grid cell  $x$ ,  $M_x$  ( $kg$ ) is the mass of grid cell  $x$ , and  $\Delta \theta_e$  is the width of the  $\theta_e$  surface.

There are five heating terms provided in the MERRA-2 product, which we can approximately relate to terms in Eq. (9), as shown in Table 1. The first three terms ( $Q_{rad}$ ,  $Q_{dyn}$ , and  $Q_{ana}$ ) can be summed to yield  $Q'_{int}$ ; the fourth ( $Q_{trb}$ ) is equal to the sum of  $Q_{diff}$  and  $Q_{sen}$ ; and the fifth ( $Q_{mst}$ ) approximates the sum of  $Q_{ice}$  and  $Q_{evap}$ . MERRA-2 does not provide terms corresponding to  $Q_{H_2O}$  or  $Q_{evap}$ , but  $Q_{mst}$  represents heating due to moist processes, which includes  $Q_{ice}$  plus water vapor evaporation and condensation within the atmosphere. This water vapor evaporation and condensation should be approximately equal to  $Q_{evap}$  with a small time lag when integrated over a  $\theta_e$  surface because mixing is preferentially along  $\theta_e$  surfaces and water vapor released into a  $\theta_e$  surface by surface evaporation will tend to transport and precipitate from the same  $\theta_e$  surface within a short time period (Bailey et al., 2019). Thus, the MERRA-2 term for heating by moist processes ( $Q_{mst}$ ) should approximate  $Q_{ice} + Q_{evap}$ .

Figure 7a compares the temporal variation in  $\dot{M}_{\theta_e}$  computed by integrating the dry air mass (i.e.,  $\theta_e$ - $M_{\theta_e}$  look-up

table) with  $M_{\theta_e}$  computed from the sum of the diabatic heating terms from MERRA-2 (via Eqs. 8 to 10). The comparison focuses on the  $\theta_e = 300$  K surface, which does not intersect with the Equator or tropopause, so the two mass flux terms ( $m_T$ ,  $m_E$ ) vanish. These two methods have a high correlation at 0.71. We do not expect perfect agreement because  $\dot{M}_{\theta_e}$  computed by the sum of heating neglects turbulent water vapor transport ( $Q_{H_2O}$ ), and only approximates  $Q_{evap}$  as discussed above. This relatively good agreement nevertheless demonstrates that the formulation based on MERRA-2 heating terms includes the dominant processes that drive temporal variations in the look-up table. Figure 7a shows poorer agreement from late August to October, which we also find in other years (Figs. S1 and S2 in the Supplement) and on lower (e.g.,  $\theta_e = 290$  K, Fig. S3) but not higher (e.g.,  $\theta_e = 310$  K, Fig. S4) surfaces, where the two methods agree better. The poor agreement may reflect a partial breakdown of the assumption that  $Q_{mst}$  approximates the sum of  $Q_{ice}$  and  $Q_{evap}$ , but further analysis is beyond the scope of this study.

Figure 7b further breaks down the sum of the heating terms in Eqs. (8) and (10) from MERRA-2 into individual components. Each term clearly displays variability on synoptic to seasonal scales. To quantify the contribution of different terms on the different timescales, we separate each term into a seasonal and synoptic component, where the seasonal component is derived by a two-harmonic fit with a constant offset and the synoptic component is the residual. We estimate the fractional contribution of each heating term on seasonal and synoptic timescales separately in Table 2, using the method in Sect. S1 in the Supplement. On the seasonal timescale, the variance is dominated by radiative heating and cooling of the atmosphere and moist processes (including both ice formation and extra water vapor from surface evaporation) together, with prominent counteraction between them. On the synoptic timescale, dissipation of the kinetic energy of turbulence dominates the variance.

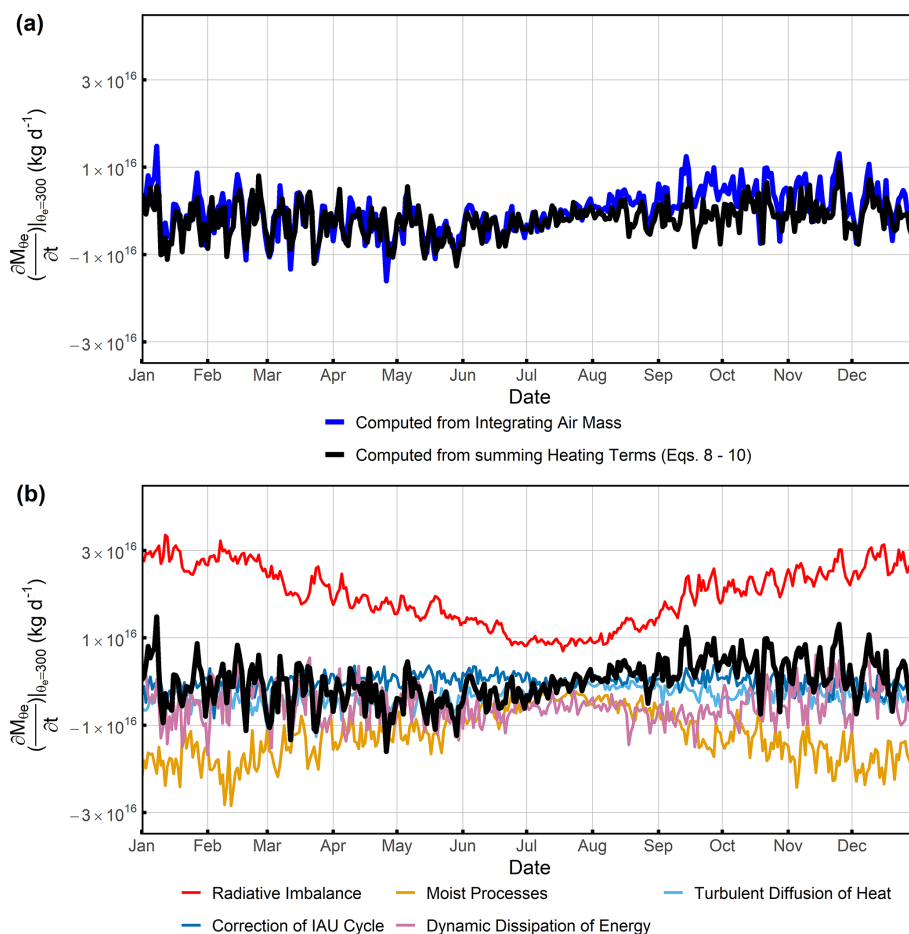
Similar analyses on different  $\theta_e$  surfaces and in different years (Figs. S1 to S4) all show that a combination of radiative heating and moist processes dominates the temporal variation in  $M_{\theta_e}$  on the seasonal timescale, while dissipation of the kinetic energy of turbulence dominates on the synoptic timescale.

#### 4 Applications of $M_{\theta_e}$ as an atmospheric coordinate

To illustrate the potential application of  $M_{\theta_e}$  for interpreting sparse data, we focus on the seasonal cycle of  $CO_2$  in the Northern Hemisphere as resolved by two series of global airborne campaigns, HIPPO and ATom. HIPPO consisted of five campaigns between 2009 and 2011, and ATom consisted of four campaigns between 2016 and 2018. Each campaign covered from  $\sim 150$  to  $\sim 14\,000$  m and from nearly pole to pole, along both northbound and southbound transects. On HIPPO, both transects were over the Pacific Ocean, while

**Table 1.** Correspondence of heating variables between our derivation (Eq. 9) and MERRA-2.

Diabatic heating terms in our derivation (Eq. 9)	Diabatic heating terms in MERRA-2, $\frac{\partial Q_i(\theta_e, t)}{\partial \theta_e}$
$Q'_{\text{int}}$	1. Radiative heating (i.e., sum of shortwave and longwave radiative heating, $Q_{\text{rad}}$ ) + 2. Absorption of kinetic energy that breaking the eddies ( $Q_{\text{dyn}}$ ) + 3. The analysis tendency introduced during the corrector segment of the incremental analysis update (IAU) cycle ( $Q_{\text{ana}}$ )
$Q_{\text{diff}} + Q_{\text{sen}}$	4. Turbulent heat flux including surface sensible heating ( $Q_{\text{trb}}$ )
$Q_{\text{evap}} + Q_{\text{ice}}$	5. Moist processes including all latent heating due to condensation and evaporation as well as to the mixing by convective parameterization ( $Q_{\text{mst}}$ )
$Q_{\text{H}_2\text{O}}$	Not available

**Figure 7.** (a) Temporal variation in  $M_{\theta_e}$  in the Northern Hemisphere at  $\theta_e = 300$  K computed by integrating air mass (blue line) and estimated from the sum of five heating terms (Table 1) in MERRA-2 (black line). (b) The heating variables are decomposed into five contributions as indicated (see Table 1). Results shown are for the year 2009.



**Table 2.** Fractional contribution of the individual heating terms in Fig. 7b to their sum for  $\theta_e = 300$  K. The analysis is done separately on synoptic and seasonal components. The seasonal component is based on a two-harmonic fit, and the synoptic component is defined as the residual. The fractional contributions sum to 1, while a positive contribution means in phase and negative contribution means anti-phase. A contribution of an absolute value that is bigger than 1 illustrates that the variability in the heating term is larger than the variability in the sum on the corresponding timescale.

Heating terms	Seasonal component	Synoptic component
$Q_{\text{rad}}$	2.25	0.03
$Q_{\text{mst}}$	-1.39	0.07
$Q_{\text{dyn}}$	0.24	0.72
$Q_{\text{dyn}}$	0.21	0.11
$Q_{\text{ana}}$	-0.31	0.07
Sum	1	1

on ATom, southbound transects were over the Pacific Ocean and northbound transects were over the Atlantic Ocean. The flight tracks are shown in Fig. 8a. We aggregate data from each campaign into northbound and southbound transects within each hemisphere but only use data from the Northern Hemisphere. We only consider tropospheric observations by excluding measurements from the stratosphere, which is defined by observed water vapor of less than 50 ppm and either  $\text{O}_3$  greater than 150 ppb or detrended  $\text{N}_2\text{O}$  to the reference year of 2009 of less than 319 ppb. Water vapor and  $\text{O}_3$  were measured by the NOAA UCATS (Unmanned Aerial Systems Chromatograph for Atmospheric Trace Species; Hurst, 2011) instrument and were interpolated to a 10 s resolution.  $\text{N}_2\text{O}$  was measured by the Harvard QCLS (Quantum Cascade Laser System; Santoni et al., 2014) instrument. Furthermore, we exclude all near-surface observations within  $\sim 100$  s of takeoffs and within  $\sim 600$  s of landings as well as missed approaches, which usually show high  $\text{CO}_2$  variability due to strong local influences. In situ measurements of  $\text{CO}_2$  were made by three different instruments on both HIPPO and Atom. Of these, we use the  $\text{CO}_2$  measurements made by the NCAR Airborne Oxygen Instrument (AO2) with a 2.5 s measurement interval (Stephens et al., 2020), for consistency with planned future applications of APO (atmospheric potential oxygen) computed from AO2. The differences between instruments are small for our application (Santoni et al., 2014). The data used in this study are averaged to a 10 s resolution, and we show the detrended  $\text{CO}_2$  values along each airborne campaign transect for the Northern Hemisphere in Fig. 8b. Since we focus on the seasonal cycle of  $\text{CO}_2$ , all airborne observations are detrended by subtracting an inter-annual trend fitted to  $\text{CO}_2$  measured at the Mauna Loa Observatory (MLO) by the Scripps  $\text{CO}_2$  Program. This trend is computed by a stiff cubic spline function plus four-harmonic

terms with linear gain to the MLO record.  $M_{\theta_e}$  is computed from ERA-Interim in this section.

#### 4.1 Mapping Northern Hemisphere $\text{CO}_2$

A conventional method to display seasonal variations in  $\text{CO}_2$  from airborne data is to plot time series of the data at a given location or latitude and different pressure levels (Graven et al., 2013; Sweeney et al., 2015). In Fig. 9, we compare this method using HIPPO and ATom airborne data, binning and averaging the data from each airborne campaign transect by pressure and latitude bins, with our new method, binning the data by pressure and  $M_{\theta_e}$ . For each latitude bin, we choose a corresponding  $M_{\theta_e}$  bin which has approximately the same meridional coverage in the lower troposphere. We remind the reader that  $M_{\theta_e}$  decreases poleward while also generally increasing with altitude (Figs. 2 to 4).

As shown in Fig. 9, the transect averages of detrended  $\text{CO}_2$  (shown as points) from both binning methods resolve well-defined seasonal cycles (based on two-harmonic fit) in all bins, with higher amplitudes near the surface (low pressure) and at high latitudes (low  $M_{\theta_e}$ ). However, binning by  $M_{\theta_e}$  leads to much smaller variations in the mean seasonal cycle (shown as solid curves) with pressure, as expected, because moist isentropes are preferential surfaces for mixing. Also, within individual pressure bins, the short-term variability relative to the mean cycles based on the distribution of all detrended observations (not shown as points but denoted as  $1\sigma$  values in Fig. 9) is smaller when binning by  $M_{\theta_e}$  ( $F$  test,  $p < 0.01$ ), except in the lower troposphere of the highest  $M_{\theta_e}$  bin ( $90 \times 10^{16}$ – $110 \times 10^{16}$  kg). The smaller short-term variability is expected because  $M_{\theta_e}$  tracks the synoptic variability in the atmosphere. When binning by latitude, the smallest short-term variability is found at the lowest bin (surface–800 mbar) and the largest short-term variability is found in the highest bin (500 mbar tropopause), except the highest latitude bin (45–55° N). When binning by  $M_{\theta_e}$ , in contrast, the short-term variability in the middle pressure bin is always smaller than the higher and lower pressure bins ( $F$  test,  $p < 0.01$ ), except for the 50-to-70  $M_{\theta_e}$  bin, where the difference between the lowest and middle pressure bins is not significant (based on  $1\sigma$  levels). The lower variability in the middle troposphere may reflect the suppression of variability from synoptic disturbances, leaving a clearer signal of the influence of surface fluxes of  $\text{CO}_2$  and stratosphere–troposphere exchanges. We compare the variance of detrended airborne observations within each  $M_{\theta_e}$ –pressure bin with its fitted value. The fitted seasonal cycle of each bin explains 63.2 % to 90.5 % of the variability for different bins, with higher fractions in the middle troposphere.

Figure 9 also shows the  $\text{CO}_2$  seasonal cycle at MLO, which falls within a single  $M_{\theta_e}$ –pressure bin ( $90 \times 10^{16}$ – $110 \times 10^{16}$  kg, 500–800 mbar) at all seasons. Although the airborne data in this bin span a wide range of latitudes ( $\sim 10$ – $75^\circ$  N), the seasonal cycle averaged over this bin is very sim-

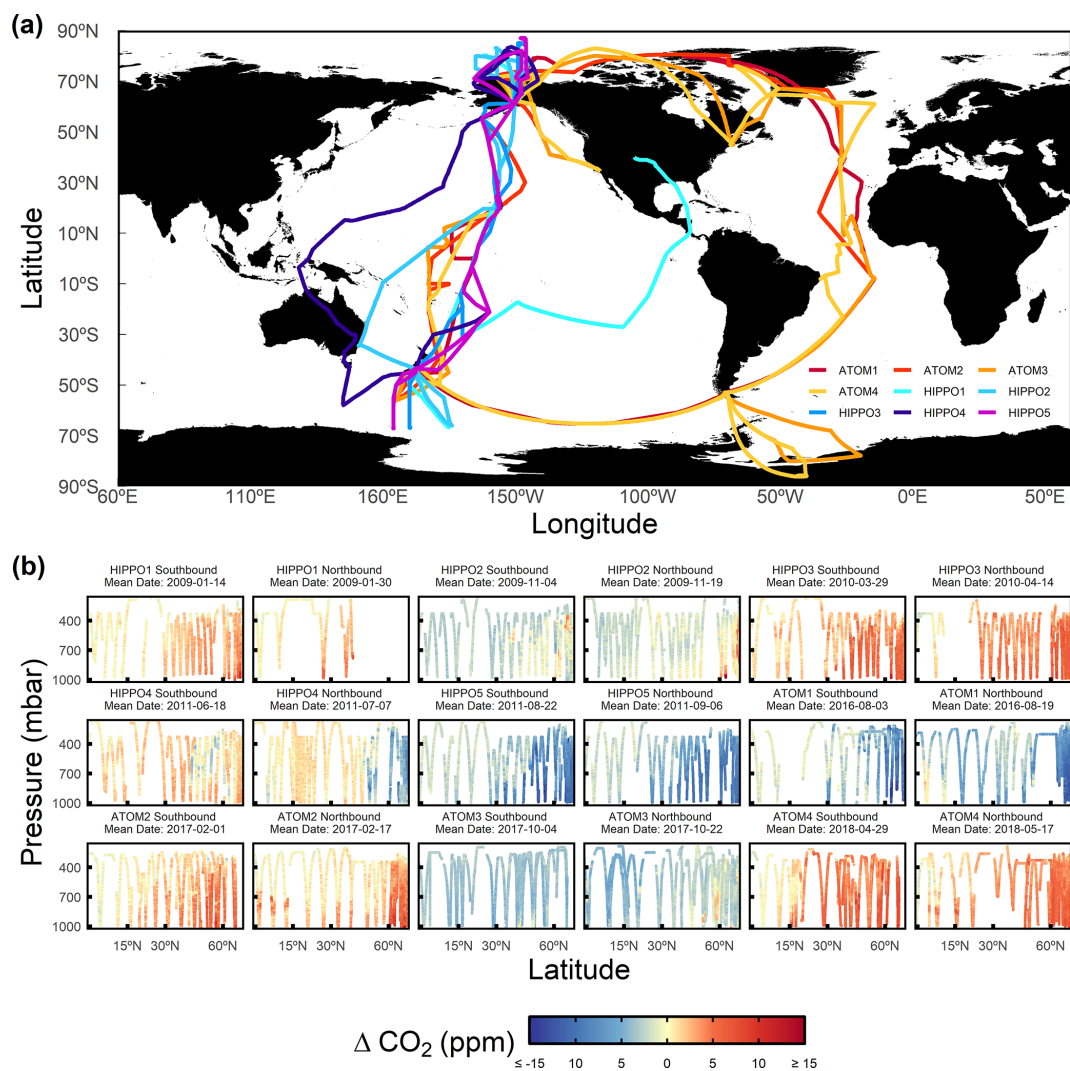


**Figure 8.** (a) HIPPO and ATom horizontal flight tracks colored by campaigns. (b) Latitude and pressure cross section of detrended CO<sub>2</sub> of each airborne campaign transect. CO<sub>2</sub> is detrended by subtracting the MLO stiff cubic spline trend, which is computed by a stiff cubic spline function plus four-harmonic functions with linear gain to the MLO record.

ilar to the cycle at MLO (airborne cycle leads by  $\sim 10$  d with 1.0% lower amplitude). This small difference is within the  $1\sigma$  uncertainty in our estimation from airborne observation, and some difference is expected, since we choose a  $M_{\theta_e}$ -pressure bin wider than the seasonal variation in  $M_{\theta_e}$  and pressure at MLO.

It is also of interest to examine how CO<sub>2</sub> data from surface stations fit into the framework based on  $M_{\theta_e}$ . Figure 10 compares the CO<sub>2</sub> seasonal cycle of five NOAA surface stations (Cooperative Global Atmospheric Data Integration Project, 2019) with the cycle from the airborne observations binned into selected  $M_{\theta_e}$  bins. These surface stations are chosen to be representative of different  $M_{\theta_e}$  ranges. For the comparison, we chose  $M_{\theta_e}$  bins that span the seasonal maximum and minimum  $M_{\theta_e}$  value of the station. These bins are narrower than the bins used in Fig. 9, in order to sharply focus

on the latitude of the station. To maximize sampling coverage, we bin the airborne data only by  $M_{\theta_e}$  without pressure sub-bins. For mid- and high-latitude surface stations (right three panels), the seasonal amplitude of station CO<sub>2</sub> and corresponding airborne CO<sub>2</sub> are close (within 4%–5%), while airborne cycles lag by 2–3 weeks. The lag presumably represents the slow mixing from the mid-latitude surface to the high-latitude mid-troposphere (Jacob, 1999). In contrast, for low-latitude stations (left two panels) which generally sample trade winds, the seasonal cycles differ significantly, indicating that the air sampled at these stations is not rapidly mixed along surfaces of constant  $M_{\theta_e}$  or  $\theta_e$  with air aloft. As mentioned above (Sect. 3.1), surfaces of high  $M_{\theta_e}$  within the Hadley circulation have two branches, one near the surface and one aloft. A timescale of several months for transport from the lower to the upper branch can be estimated from

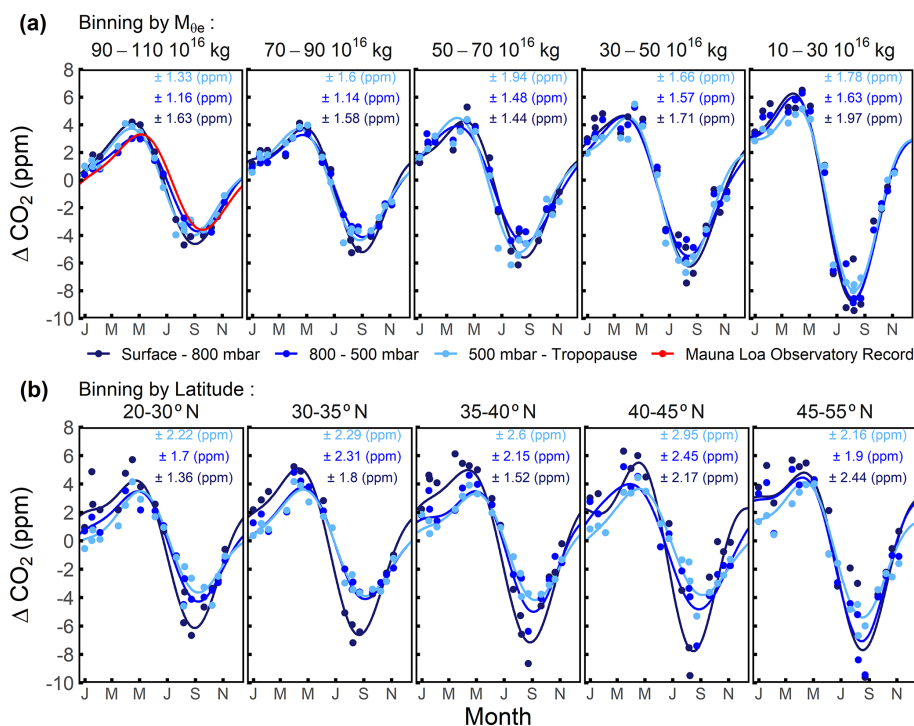


**Figure 9.** Seasonal cycles of airborne Northern Hemisphere CO<sub>2</sub> data sorted by (a)  $M_{\theta_e}$ –pressure bins and (b) latitude–pressure bins.  $M_{\theta_e}$  bins ( $10^{16}$  kg) and latitude bins are shown at the top of each panel. Pressure bins are colored. The latitude bounds are chosen to approximate the meridional coverage of each corresponding  $M_{\theta_e}$  bin in the lower troposphere. The seasonal cycle at MLO from 2009 to 2018 is shown in the 90–110  $M_{\theta_e}$  bin panel, which spans the  $M_{\theta_e}$  of the station. Airborne observations are first grouped into  $M_{\theta_e}$ –pressure or latitude–pressure bins and then averaged for each airborne campaign transect, shown as points. We filter out the points averaged from fewer than twenty 10 s observations. The seasonal cycle of airborne data and MLO (2009–2018) are computed by a two-harmonic fit to the detrended time series. The  $1\sigma$  variability about the seasonal cycle fits for each  $M_{\theta_e}$ –pressure or latitude–pressure bin is labeled at the top of each panel. These  $1\sigma$  values are based on the distribution of all binned observations (not shown), rather than on the distribution of average CO<sub>2</sub> of each bin and airborne campaign transect (shown).

the known overturning flows based on air mass flux stream functions (Dima and Wallace, 2003). This delay, plus strong mixing and diabatic effects (Miyazaki et al., 2008), ensures that the lower and upper branches are not well connected on seasonal timescales. Our results nevertheless demonstrate that the  $M_{\theta_e}$  framework combining airborne and surface data could help understanding of details of atmospheric transport both along and across  $\theta_e$  surfaces.

#### 4.2 Computing the hemispheric mass-weighted average CO<sub>2</sub> mole fraction

We next illustrate the use of  $M_{\theta_e}$  for computing the mass-weighted average of a long-lived chemical tracer by performing this exercise for CO<sub>2</sub> in the Northern Hemisphere. We calculate the Northern Hemisphere tropospheric mass-weighted average CO<sub>2</sub> from each airborne transect using a method that assumes that CO<sub>2</sub> is uniformly mixed on  $\theta_e$  surfaces throughout the hemisphere (Barnes et al., 2016; Parazoo et al., 2011, 2012). We exclude airborne observation from HIPPO-1 Northbound due to the lack of data north of

40° N. We use the  $\theta_e$ – $M_{\theta_e}$  look-up table of the corresponding date to assign a value of  $M_{\theta_e}$  to each observation based on its  $\theta_e$ . The observations for each transect are then sorted by  $M_{\theta_e}$ . The hemispheric average CO<sub>2</sub> is calculated by trapezoidal integration of CO<sub>2</sub> as a function of  $M_{\theta_e}$  and divided by the total dry air mass as computed from the corresponding range of  $M_{\theta_e}$ .

To illustrate the  $M_{\theta_e}$  integration method, we choose HIPPO-1 Southbound and show CO<sub>2</sub> measurements and  $\Delta$ CO<sub>2</sub> atmospheric inventory (Pg) as a function of  $M_{\theta_e}$  in Fig. 11. The Northern Hemisphere tropospheric average detrended  $\Delta$ CO<sub>2</sub> is computed by integrating the area under the curve (subtracting negative contributions) and dividing by the maximum value of  $M_{\theta_e}$  within the hemisphere (here  $195.13 \times 10^{16}$  kg). This yields a mass-weighted average detrended  $\Delta$ CO<sub>2</sub> of 1.13 ppm for the full troposphere of the Northern Hemisphere. The trapezoidal integration has a high accuracy because the data are dense over  $M_{\theta_e}$ . The  $\Delta$ CO<sub>2</sub> atmospheric inventory is dominated by the domain  $M_{\theta_e} < 120 \times 10^{16}$  kg (mid-latitude to high latitude), which has a large CO<sub>2</sub> seasonal cycle driven by a temperate and

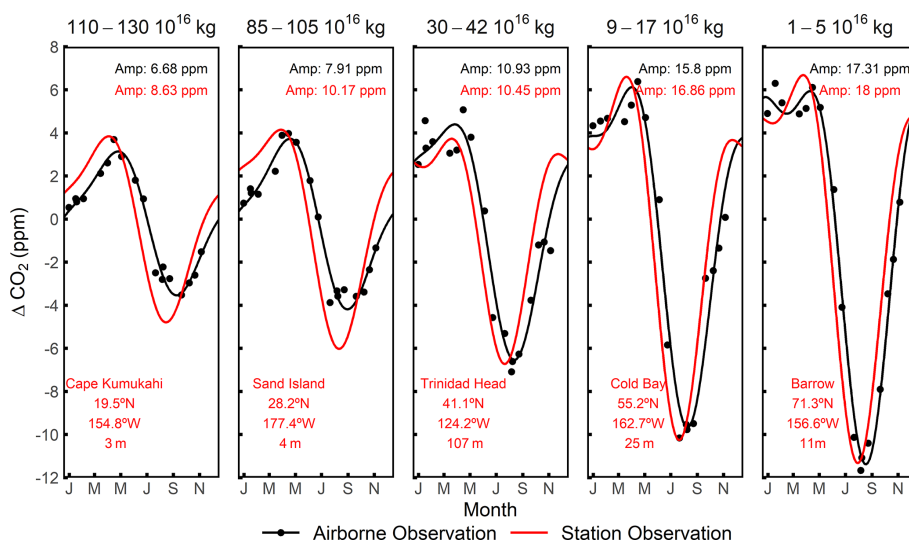


**Figure 10.** CO<sub>2</sub> seasonal cycles of multiple surface stations (2009–2018) compared to seasonal cycles of airborne observations averaged over corresponding  $M_{\theta_e}$  bin. The choice of  $M_{\theta_e}$  bin is to approximate the range of  $M_{\theta_e}$  at each corresponding surface station and is shown at the top of each panel. Daily  $M_{\theta_e}$  of the station is computed from ERA-Interim, based on its location. We detrend station and airborne observations by subtracting the MLO stiff cubic spline trend. We compute average detrended CO<sub>2</sub> for each airborne campaign transect and each  $M_{\theta_e}$  bin, shown as black points. The seasonal cycles are computed from a two-harmonic fit, with the seasonal amplitude (Amp) shown in the upper right of each panel.

boreal ecosystem, with less than 4.1 % contributed by the additional  $\sim 38.8$  % of the air mass outside this domain in the low latitudes or upper troposphere (Fig. 11b), where  $\Delta\text{CO}_2$  differs less from the subtracted baseline.

We compute Northern Hemisphere mass-weighted average detrended  $\Delta\text{CO}_2$  for each airborne campaign transect and fit the time series to a two-harmonic fit to estimate the seasonal cycle (Fig. 12). We find that the cycle has a seasonal amplitude of 7.9 ppm and a downward zero-crossing on Julian day 179, where the latter is defined as the date when the detrended seasonal cycle changes from positive to negative.

To address the error in our estimation of the Northern Hemisphere mass-weighted average CO<sub>2</sub> seasonal cycle from HIPPO and Atom airborne observation, we consider two main sources: (1) irreproducibility in the CO<sub>2</sub> measurements and (2) limited coverage in space and time. For the first contribution, we compute the difference between mass-weighted average CO<sub>2</sub> from AO2 and mean mass-weighted average CO<sub>2</sub> from Harvard QCLS, Harvard OMS, and NOAA Picarro for each airborne campaign transect, while masking values that are missing in any of these datasets. We compute the standard deviation of these differences ( $\pm 0.15$  ppm) for the mass-weighted average CO<sub>2</sub> of each airborne campaign transect as the  $1\sigma$  level of uncertainty. We further compute the uncertainties for the seasonal amplitude of  $\pm 0.11$  ppm and for the downward zero-crossing of  $\pm 0.83$  d, which are calculated from 1000 iterations of the two-harmonic fit, allowing for random Gaussian uncertainty ( $\sigma = \pm 0.15$  ppm) for each transect.

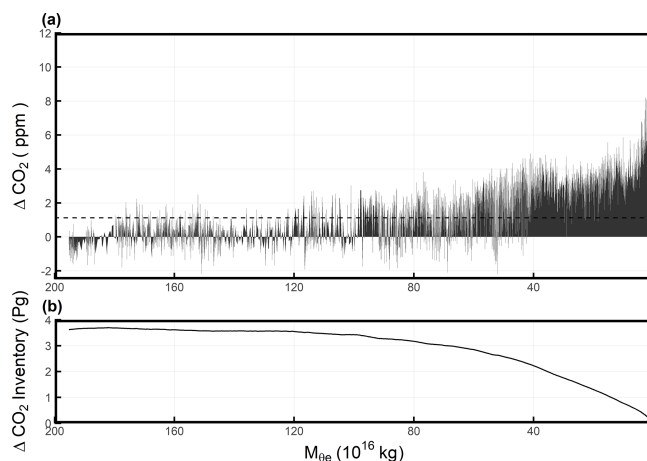


**Figure 11.** (a) Detrended CO<sub>2</sub> measurements from HIPPO-1 Southbound (from 12 to 17 January 2009) plotted as a function of  $M_{\theta_e}$  in the Northern Hemisphere. The data are detrended by subtracting the MLO stiff cubic spline trend. Individual points are connected by straight line segments, and the area under the resulting curve is shaded. We note that the area under the curve has units of parts per million  $\times$  kilograms, and dividing this by the total dry air mass (i.e., the range of  $M_{\theta_e}$  of the integral) gives the parts per million unit because the mass of dry air is proportional to the moles of dry air. The Northern Hemisphere average of 1.13 ppm is indicated by the dashed line. (b) Integral of the data in panel (a), rescaled from parts per million to petagrams, integrating from  $M_{\theta_e} = 0$  to a given  $M_{\theta_e}$  value.

**Table 3.** RMSE, seasonal amplitude, and day of year of the downward zero-crossing of each simulation based on the Jena CO<sub>2</sub> inversion. The true value (daily average CO<sub>2</sub>) is computed by integrating over all tropospheric grid cells of the Jena CO<sub>2</sub> inversion, while troposphere is defined by PVU < 2 from ERA-Interim. Seasonal amplitude and downward zero-crossing of true average and each simulation is computed from two-harmonic fit to the detrended value, which is detrended by subtracting the MLO cubic stiff spline. Subsampling with randomly retaining a certain fraction of data are conducted by randomly subsampling 1000 times, thus, the seasonal amplitude and day of year of the downward zero-crossing is computed as the mean ± standard deviation of the 1000 iterations.

Method	RMSE (ppm)*	Seasonal amplitude (ppm)	Downward zero-crossing (day)
True value (cutoff at PVU = 2)	–	7.58	175.1
Evaluation of $M_{\theta_e}$ integration method			
Full airborne coverage	0.30	7.65	181.1
Subsample: Equator to 30° N	1.26	5.74	197.8
Subsample: poleward of 30° N	0.82	9.47	179.0
Subsample: surface–600 mbar	0.57	7.77	185.1
Subsample: 600 mbar–tropopause	0.38	7.28	180.7
Subsample: Pacific only	0.33	7.33	181.6
Subsample: randomly retain 10 %	0.38	7.64 ± 0.116	182.4 ± 0.82
Subsample: randomly retain 5 %	0.40	7.65 ± 0.163	182.3 ± 1.08
Subsample: randomly retain 1 %	0.56	7.72 ± 0.366	182.2 ± 2.24
Subsample: Medusa coverage	0.48	7.52	181.7
Evaluation of latitude–pressure weighted average method			
Full airborne coverage	0.68	9.16	182.2

\* Each simulation yields 17 data points of different dates over the seasonal cycle from 17 airborne campaign transects. RMSE of each simulation is computed with respect to the true value.

For the contribution to the error in the amplitude and phase from limited spatial and temporal coverage, we use simulated CO<sub>2</sub> data from the Jena CO<sub>2</sub> inversion Run ID s04oc v4.3 (Rödenbeck et al., 2003). This model includes full atmospheric fields from 2009 to 2018, which we detrend using the cubic spline fit to the observed MLO trend. From these detrended fields, we compute the climatological cycle of the Northern Hemisphere average by integrating over all tropospheric grid cells (cutoff at PVU = 2) to produce a daily time series of the hemispheric mean, which we take as the model “truth”. We fit a two-harmonic function to this true time series to compute a true climatological cycle over the 2009–2018 period (Table 3), which is our target for validation. We then subsample the Jena CO<sub>2</sub> inversion along the HIPPO and ATom flight tracks and process the data similarly to the observations, using the  $M_{\theta_e}$  integration method and a two-harmonic fit. The comparison shows that the  $M_{\theta_e}$  integration method yields an amplitude which is 1 % too large and yields a downward zero-crossing date which is 6 d too late. We view these offsets as systematic biases, which we correct from the observed amplitude and phase reported above. The uncertainties in these biases are hard to quantify, but we take ±100 % as a conservative estimate. We thus allow an additional random error of ±0.08 ppm in amplitude and ±6.0 d in downward zero-crossing for uncertainty in the bias. Combining the random and systematic error contributions leads to a corrected Northern Hemisphere tropospheric

average CO<sub>2</sub> seasonal cycle amplitude of  $7.8 \pm 0.14$  ppm and downward zero-crossing of  $173 \pm 6.1$  d. This corrected cycle is an estimate of the climatological average from 2009 to 2018.

The error due to limited spatial and temporal coverage can be divided into three components: limited seasonal coverage (17 transects over the climatological year), limited interannual coverage (sampling particular years instead of all years), and limited spatial coverage (under-sampling the full hemisphere). We quantify the combined biases due to both limited seasonal and limited interannual coverage by comparing the two-harmonic fit of the full true daily time series of the hemispheric mean to a two-harmonic fit of those data subsampled on the actual mean sampling dates of the 17 flight tracks. We isolate the bias associated with limited seasonal coverage by repeating this calculation, replacing the true daily time series with the daily climatological cycle. The bias associated with limited spatial coverage is quantified as the residual. Combining these results, we estimate that the limited seasonal, interannual, and spatial coverage account for biases in the downward zero-crossing of 1.1, 1.4, and 3.5 d respectively, all in the same direction (too late). The seasonal amplitude biases due to individual components are all small (< 0.5 %).

It is of interest to compare our estimate of the Northern Hemisphere average cycle with the cycle at Mauna Loa, which is also broadly representative of the hemisphere. Our comparison in Fig. 12 shows small but significant differences

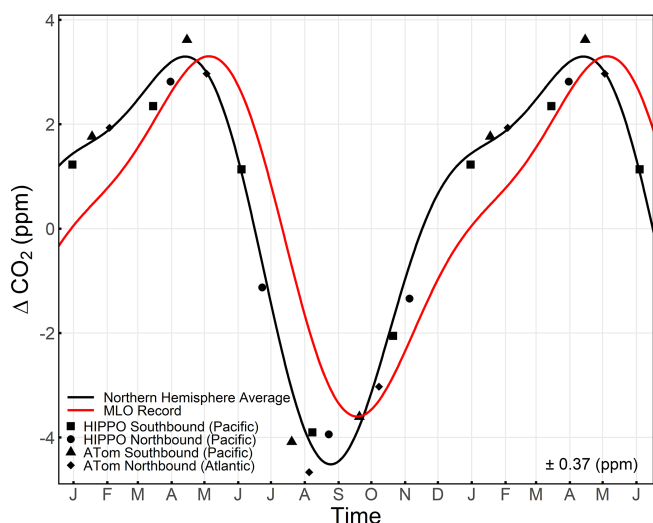


**Figure 12.** Comparison between the CO<sub>2</sub> seasonal cycle of Northern Hemisphere tropospheric average computed from airborne observation and the  $M_{\theta_e}$  integration method (black points and line) and the mean cycle at MLO measured by Scripps CO<sub>2</sub> Program from 2009 to 2018 (red line). Both are detrended by subtracting a stiff cubic spline trend at MLO. We then compute mass-weighted average detrended CO<sub>2</sub> for each airborne campaign transect, shown as black points, with campaigns and transects presented as different shapes. The seasonal cycle of both are computed by a two-harmonic fit to the detrended time series. The  $1\sigma$  variability in the detrended average CO<sub>2</sub> values about the fit line is shown on the lower right. The first half year is repeated for clarity.

in both amplitude and phase, with the MLO amplitude being  $\sim 11.5\%$  smaller than the hemispheric average and lagging in phase by  $\sim 1$  month. There are also differences in the shape of the cycle, with the MLO cycle rising more slowly from October to February but more quickly from February to May. These features at least partly reflect variations in the transport of air masses to the station (Harris et al., 1992; Harris and Kahl, 1990).

In Fig. 13, we compare the  $M_{\theta_e}$  integration method with an alternate latitude–pressure weighted average method, with no correction for synoptic variability. For this method, we bin flight track subsampled Jena CO<sub>2</sub> inversion data into  $\sin(\text{latitude})$ -pressure bins with 0.01 and 25 mbar as intervals respectively, while all bins without data are filtered. We further compute weighted average CO<sub>2</sub> for each airborne campaign transect. The root-mean-square errors (RMSEs) to the true average of the  $M_{\theta_e}$  integration method are  $\pm 0.32$  and  $\pm 0.27$  ppm for the HIPPO and ATom campaigns respectively, which are smaller than the RMSEs of the simple latitude–pressure weighted average method at  $\pm 0.82$  and  $\pm 0.53$  ppm.

We also evaluate the biases in the hemispheric average seasonal cycles computed with the simple latitude–pressure weighted average method. As summarized in Table 3, the latitude–pressure weighted average method yields a larger

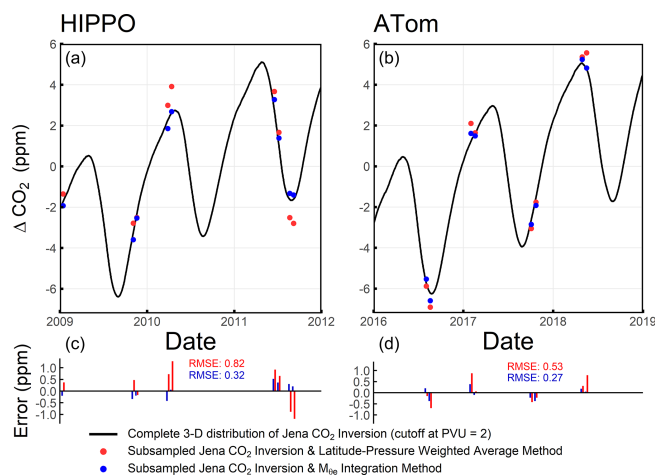


**Figure 13.** Comparison between the Northern Hemisphere average CO<sub>2</sub> from full integration of the simulated atmospheric fields from the Jena CO<sub>2</sub> inversion (cutoff at PVU = 2) and from two methods that use the same simulated data subsampled with HIPPO or ATom coverage: (1) the  $M_{\theta_e}$  integration method (blue) and (2) simple integration by  $\sin(\text{latitude})$ -pressure (red). We divide the comparison into HIPPO (a, c) and ATom (b, d) temporal coverage. Panels (c) and (d) show the error for individual tracks using alternate subsampling methods.

error in seasonal amplitude ( $M_{\theta_e}$  method 1.0% too large, latitude–pressure method 20.8% too large), while both methods show a similar phasing error (6 to 7 d late). The larger error associated with the latitude–pressure weighted average method is consistent with strong influence of synoptic variability. This synoptic variability could potentially be corrected using model simulations of the 3-dimensional CO<sub>2</sub> fields (Bent, 2014). The  $M_{\theta_e}$  integration method appears advantageous because it accounts for synoptic variability and easily yields a hemispheric average by directly integrating over  $M_{\theta_e}$ .

The relative success of the  $M_{\theta_e}$  integration method in yielding accurate hemispheric averages using HIPPO and ATom data is attributable partly to the extensive data coverage. To explore the coverage requirement for reliably resolving hemispheric averages, we also test the integration method when applied to simulated data with lower coverage. We start with the same coverage as for ATom and HIPPO but select only subsets of the points in four groups: poleward of 30° N, Equator to 30° N, surface to 600 mbar, and 600 mbar to tropopause. We also examine whether we can only utilize observation along the Pacific transect by excluding measurements along the Atlantic transects (ATom northbound). We further explore the impact of reduced sampling density by subsampling the Jena CO<sub>2</sub> inversion based on the spatial coverage of the Medusa sampler, which is an airborne flask sampler that collected 32 cryogenically dried air samples per flight during HIPPO and ATom (Stephens et al., 2020). We further randomly retain 10%, 5%, and 1% of

the full flight track subsampled data, repeating each ratio with 1000 iterations. We compute the detrended average CO<sub>2</sub> from these nine simulations by the  $M_{\theta_e}$  integration method and then compute the RMSE relative to the detrended true hemispheric average, together with the seasonal magnitude and day of year of the downward zero-crossing, as summarized in Table 3. HIPPO-1 Northbound is excluded in all these simulations. The number of data points of each simulation and number of observations of the original HIPPO and ATom datasets are summarized in Table S1. These results show that limiting sampling to either equatorward or poleward of 30° N yields significant error (24.3 % smaller and 24.9 % larger seasonal amplitude respectively). Additionally, there is a  $\sim 25$  d lag in phase if sampling is limited to equatorward of 30° N. However, restricting sampling to be exclusively above or below 600 mbar or only along the Pacific transect does not lead to significant errors. Randomly reducing the sampling by 10- to 100-fold or only keeping Medusa spatial coverage also has minimal impact. This suggests that, to compute the average CO<sub>2</sub> of a given region, it may be sufficient to have low sampling density provided that the measurements adequately cover the full range in  $\theta_e$  (or  $M_{\theta_e}$ ).

## 5 Discussion and summary

We have presented a transformed isentropic coordinate,  $M_{\theta_e}$ , which is the total dry air mass under a given  $\theta_e$  surface in the troposphere of the hemisphere.  $M_{\theta_e}$  can be computed from meteorological fields by integrating dry air mass under a specific  $\theta_e$  surface, and different reanalysis products show a high consistency. The  $\theta_e$ – $M_{\theta_e}$  relationship varies seasonally due to seasonal heating and cooling of the atmosphere via radiative heating and moist processes. The seasonality in the relationship is greater at low  $\theta_e$  compared to high  $\theta_e$  and is greater in the Northern Hemisphere than in the Southern Hemisphere. The  $\theta_e$ – $M_{\theta_e}$  relationship also shows synoptic-scale variability, which is mainly driven by the dissipation of the kinetic energy of turbulence.  $M_{\theta_e}$  surfaces show much less seasonal displacement with latitude and altitude than surfaces of constant  $\theta_e$  while being parallel and exhibiting essentially identical synoptic-scale variability. As a coordinate for mapping tracer distributions,  $M_{\theta_e}$  shares with  $\theta_e$  the advantages of following displacements due to synoptic disturbances and aligning with surfaces of rapid mixing.  $M_{\theta_e}$  has the additional advantages of being approximately fixed in space seasonally, which allows mapping to be done on seasonal timescales, and having units of mass, which provides a close connection with atmospheric inventories.

As a coordinate,  $M_{\theta_e}$  is probably better viewed as an alternative to latitude, due to its nearly fixed relationship with latitude over season, rather than as an alternative to altitude (or pressure), as typically done for potential temperature (Miyazaki et al., 2008; Miyazaki and Iwasaki, 2005; Parazoo et al., 2011; Tung, 1982; Yang et al., 2016). Even though the

contours of constant  $M_{\theta_e}$  extend over a wide range of latitudes (from low latitudes at the Earth's surface to high latitudes aloft), a close association with latitude is provided by the point of contact with the Earth's surface. Also,  $M_{\theta_e}$  is nearly always monotonic with latitude (increasing equatorward), while it is not necessarily monotonic with altitude in the lower troposphere (Figs. 2 and 3).

As a first application, we have illustrated using  $M_{\theta_e}$  the seasonal variation in CO<sub>2</sub> in the Northern Hemisphere, with data from the HIPPO and ATom airborne campaigns. This application shows that  $M_{\theta_e}$  has several advantages as a coordinate compared to using latitude: (1) variations in CO<sub>2</sub> with pressure are smaller at fixed  $M_{\theta_e}$  than at fixed latitude, and (2) the scatter about the mean CO<sub>2</sub> seasonal cycle is smaller when sorting data into pressure– $M_{\theta_e}$  bins than into pressure–latitude bins. We have also shown that, at middle and high latitudes, the CO<sub>2</sub> seasonal cycles that are resolved in the airborne data (binned by  $M_{\theta_e}$  but not pressure) are very similar to the cycles observed at surface stations at the appropriate latitude, with a phase lag of  $\sim 2$  to 3 weeks. At lower latitudes, CO<sub>2</sub> cycles in the airborne data (binned similarly by  $M_{\theta_e}$ ) are less consistent with surface data, as expected due to slow transport and diabatic processes within the Hadley circulation. For characterizing the patterns of variability in airborne CO<sub>2</sub> data, we expect the advantages of  $M_{\theta_e}$  over latitude will be greatest for sparse datasets, allowing data to be binned more coarsely with pressure or elevation while still resolving features of large-scale variability, such as seasonal cycles or gradients with latitude.

As a second application, we use  $M_{\theta_e}$  to compute the Northern Hemisphere tropospheric average CO<sub>2</sub> from the HIPPO and ATom airborne campaigns by integrating CO<sub>2</sub> over  $M_{\theta_e}$  surfaces. With a small correction for systematic biases induced by limited hemispheric coverage of the HIPPO and ATom flight tracks, we report a seasonal amplitude of  $7.8 \pm 0.14$  ppm and a downward zero-crossing on Julian day  $173 \pm 6.1$ . This hemispheric average cycle may prove valuable as a target for validation of models of surface CO<sub>2</sub> exchange.

Our analysis also clarifies that computing hemispheric averages with the  $M_{\theta_e}$  integration method depends on adequate spatial coverage. The coverage provided by the HIPPO and ATom campaigns appears more than adequate for computing the average seasonal cycle of CO<sub>2</sub> in the Northern Hemisphere, and the errors for this application remain small if the coverage is limited to either above or below 600 mbar or reduced to retain only 1 % of the measurements. Most critical is maintaining coverage in latitude or  $M_{\theta_e}$  surfaces. The  $M_{\theta_e}$  integration method of computing hemispheric averages assumes that the tracer is uniformly distributed and instantly mixed on  $\theta_e$  ( $M_{\theta_e}$ ) surfaces. We have shown that systematic gradients in CO<sub>2</sub> are resolved with pressure at fixed  $M_{\theta_e}$ , which reflects the finite rates of dispersion on  $\theta_e$  surfaces. Further improvements to the integration method seem possible by integrating separately over different pressure lev-

els, taking account of the different mass fraction in different pressure bins (e.g., Fig. 5). The need is especially relevant for high  $M_{\theta_e}$  bins which are less completely mixed and which tend to intersect the Equator or have separate surface branches. For these  $M_{\theta_e}$  bins, it would be more appropriate to integrate over  $M_{\theta}$  in the upper and lower atmosphere separately. This complication is of minor importance for computing the mass-weighted average CO<sub>2</sub> cycle, because the cycle of CO<sub>2</sub> is small in these air masses.

The definition of  $M_{\theta_e}$  requires horizontal and vertical boundaries for the integration of dry air masses. We use the dynamic tropopause (based on potential vorticity units) and the Equator as boundaries, which is appropriate for integrating tropospheric inventories in a hemisphere. Other boundaries may be more appropriate for other applications. For example,  $M_{\theta_e}$  could be computed from the lowest  $\theta_e$  surface in the Southern Hemisphere with a latitude cutoff at 30° S, to apply to airborne observations only over the Southern Ocean. On the other hand, the boundary choice only influences  $M_{\theta_e}$  surfaces that actually intercept the boundaries, making the choice less important at high latitudes in the lower troposphere (lowest  $M_{\theta_e}$  surfaces). Some tropospheric applications may also benefit by integrating over dry potential temperature ( $\theta$ ) rather than  $\theta_e$ .

Based on our promising results for CO<sub>2</sub>, we expect that  $M_{\theta_e}$  may be usefully applied as a coordinate for mapping and computing atmospheric inventories of many tracers, such as O<sub>2</sub> / N<sub>2</sub>, N<sub>2</sub>O, CH<sub>4</sub>, and the isotopes of CO<sub>2</sub>, whose residence time is long compared to the timescale for mixing along isentropes.  $M_{\theta_e}$  may also prove useful in the design phase of airborne campaigns to ensure strategic coverage. Our results show that, to study the seasonal cycle of a tracer on a hemispheric scale, it is critical to have well-distributed sampling in  $M_{\theta_e}$ .



**Appendix A: Temporal variation in  $M_\theta$**

Following Walin’s derivation for cross-isothermal volume flow in the ocean (Walin, 1982), we show how  $\dot{M}_\theta = \frac{\partial}{\partial t} M_\theta(\theta_e, t)$  can be related to energy and mass fluxes. We start by deriving the relationship for  $M_\theta$  (based on potential temperature  $\theta$ ) but later generalize to apply to  $M_{\theta_e}$ .

All definitions are summarized in Table A1, and Fig. A1 is the schematic diagram of mass and energy flux.

All mass and heat fluxes into region  $R(\theta, t)$  are counted as positive. The heat fluxes through the tropopause, Equator, and surface of region  $R(\theta, t)$  can be divided into an advective ( $F(\theta, t)$ ) and a turbulent ( $D(\theta, t)$ ) component. Integrating over the tropopause and equatorial boundary, we have

$$Q_T(\theta, t) = C_{pd} \int_{-\infty}^{\theta} \frac{\partial F_T(\theta', t)}{\partial \theta'} \theta' d\theta' + \int_{-\infty}^{\theta} \frac{\partial D_T(\theta', t)}{\partial \theta'} d\theta', \quad (A1)$$

$$Q_E(\theta, t) = C_{pd} \int_{-\infty}^{\theta} \frac{\partial F_E(\theta', t)}{\partial \theta'} \theta' d\theta' + \int_{-\infty}^{\theta} \frac{\partial D_E(\theta', t)}{\partial \theta'} d\theta', \quad (A2)$$

$$Q_I(\theta, t) = C_{pd} \cdot F_I(\theta, t) \cdot \theta + D_I(\theta, t), \quad (A3)$$

where  $C_{pd}$  is the heat capacity of dry air in units of  $\text{J kg}^{-1} \text{K}^{-1}$ .

Based on the continuity of mass and energy for region  $R(\theta, t)$ , we obtain

$$\begin{aligned} \frac{\partial}{\partial t} M_\theta(\theta, t) &= F_T(\theta, t) + F_E(\theta, t) + F_I(\theta, t) \\ &= \int_{-\infty}^{\theta} \frac{\partial F_T(\theta', t)}{\partial \theta'} d\theta' + \int_{-\infty}^{\theta} \frac{\partial F_E(\theta', t)}{\partial \theta'} d\theta' \\ &\quad + F_I(\theta, t), \end{aligned} \quad (A4)$$

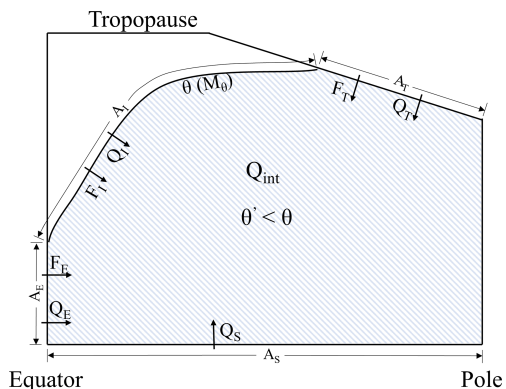


**Figure A1.** Illustration of terms defined in Table A1. Shaded area denotes the region  $R(\theta, t)$  with  $\theta'$  lower than  $\theta$ , which is the area of mass integration to yield  $M_\theta$ . The curve denotes a given  $\theta$  or  $M_\theta$  surface.

$$\begin{aligned} C_{pd} \frac{\partial}{\partial t} \int_{-\infty}^{\theta} \frac{\partial M_\theta(\theta', t)}{\partial \theta'} \theta' d\theta' &= Q_T(\theta, t) + Q_E(\theta, t) \\ &\quad + Q_I(\theta, t) + \int_{-\infty}^{\theta} \frac{\partial Q_s(\theta', t)}{\partial \theta'} d\theta' \\ &\quad + \int_{-\infty}^{\theta} \frac{\partial Q_{int}(\theta', t)}{\partial \theta'} d\theta'. \end{aligned} \quad (A5)$$

Substituting Eqs. (A1) to (A3) into Eq. (A5) and differentiating with respect to  $\theta$  yields

$$\begin{aligned} C_{pd} \theta \frac{\partial}{\partial t} \frac{\partial M_\theta(\theta, t)}{\partial \theta} &= C_{pd} \theta \left( \frac{\partial F_T(\theta, t)}{\partial \theta} + \frac{\partial F_E(\theta, t)}{\partial \theta} \right. \\ &\quad \left. + \frac{\partial F_I(\theta, t)}{\partial \theta} \right) + C_{pd} F_I(\theta, t) + \frac{\partial Q_{diff}(\theta, t)}{\partial \theta} \\ &\quad + \frac{\partial Q_s(\theta, t)}{\partial \theta} + \frac{\partial Q_{int}(\theta, t)}{\partial \theta}, \end{aligned} \quad (A6)$$

where

$$\begin{aligned} Q_{diff}(\theta, t) &= \int_{-\infty}^{\theta} \frac{\partial D_T(\theta', t)}{\partial \theta'} d\theta' + \int_{-\infty}^{\theta} \frac{\partial D_E(\theta', t)}{\partial \theta'} d\theta' \\ &\quad + D_I(\theta, t). \end{aligned} \quad (A7)$$

Differentiating Eq. (A4) with respect to  $\theta$  and multiplying  $C_{pd} \cdot \theta$  yields

$$\begin{aligned} C_{pd} \theta \frac{\partial}{\partial t} \frac{\partial M_\theta(\theta, t)}{\partial \theta} &= C_{pd} \theta \left( \frac{\partial F_T(\theta, t)}{\partial \theta} + \frac{\partial F_E(\theta, t)}{\partial \theta} \right. \\ &\quad \left. + \frac{\partial F_I(\theta, t)}{\partial \theta} \right). \end{aligned} \quad (A8)$$

Subtracting Eq. (A8) from Eq. (A6), we obtain

$$\begin{aligned} C_{pd} F_I(\theta, t) &= - \frac{\partial Q_{diff}(\theta, t)}{\partial \theta} - \frac{\partial Q_s(\theta, t)}{\partial \theta} \\ &\quad - \frac{\partial Q_{int}(\theta, t)}{\partial \theta}. \end{aligned} \quad (A9)$$

Equation (A9) divided by  $C_{pd}$  plus Eq. (A4) yields

$$\begin{aligned} \frac{\partial}{\partial t} M_\theta(\theta, t) &= - \frac{1}{C_{pd}} \left( \frac{\partial Q_{diff}(\theta, t)}{\partial \theta} + \frac{\partial Q_s(\theta, t)}{\partial \theta} \right. \\ &\quad \left. + \frac{\partial Q_{int}(\theta, t)}{\partial \theta} \right) + \int_{-\infty}^{\theta} \frac{\partial F_T(\theta', t)}{\partial \theta'} d\theta' \\ &\quad + \int_{-\infty}^{\theta} \frac{\partial F_E(\theta', t)}{\partial \theta'} d\theta'. \end{aligned} \quad (A10)$$

Equation (A10) illustrates the temporal variation in  $M_\theta$ , where  $Q_{int}$  includes radiative heating (i.e., sum of shortwave

**Table A1.** Definition of variables.

Variable	Definition	Unit
$\theta'(r, t)$	Potential temperature at location $r$ and time $t$ .	K
$\theta$	Potential temperature of the chosen isentropic surface.	K
$R(\theta, t)$	A region in which $\theta'(r, t) < \theta$ , shown as shaded area in Fig. A1.	
$A_T(\theta, t)$	Area at the tropopause where $\theta'(r, t) < \theta$ .	m <sup>2</sup>
$A_E(\theta, t)$	Area at the Equator where $\theta'(r, t) < \theta$ .	m <sup>2</sup>
$A_I(\theta, t)$	Area where $\theta'(r, t) = \theta$ .	m <sup>2</sup>
$A_S(\theta, t)$	Area at the Earth surface where $\theta'(r, t) < \theta$ .	m <sup>2</sup>
$M_\theta(\theta, t)$	Dry air mass of $R(\theta, t)$ .	kg
$F_T(\theta, t)$	Mass flux through $A_T(\theta, t)$ . Positive value denotes flux into region $R(\theta, t)$ .	kg s <sup>-1</sup>
$F_E(\theta, t)$	Mass flux through $A_E(\theta, t)$ . Positive value denotes flux into region $R(\theta, t)$ .	kg s <sup>-1</sup>
$F_I(\theta, t)$	Mass flux through $A_I(\theta, t)$ . Positive value denotes flux into region $R(\theta, t)$ .	kg s <sup>-1</sup>
$Q_T(\theta, t)$	Heat flux through $A_T(\theta, t)$ . Positive value denotes flux into region $R(\theta, t)$ .	J s <sup>-1</sup>
$Q_E(\theta, t)$	Heat flux through $A_E(\theta, t)$ . Positive value denotes flux into region $R(\theta, t)$ .	J s <sup>-1</sup>
$Q_I(\theta, t)$	Heat flux through $A_I(\theta, t)$ . Positive value denotes flux into region $R(\theta, t)$ .	J s <sup>-1</sup>
$Q_S(\theta, t)$	Surface sensible heat flux to the region $R(\theta, t)$ . Positive value denotes flux into the atmosphere.	J s <sup>-1</sup>
$Q_{\text{int}}(\theta, t)$	Internal heating and cooling within region $R(\theta, t)$ . Positive value denotes absorbing heat.	J s <sup>-1</sup>
$\frac{\partial Q_S(\theta, t)}{\partial \theta}$	Surface sensible heat flux to the $\theta$ surface. Positive value denotes flux into the atmosphere (i.e., $\theta$ surface).	J s <sup>-1</sup> K <sup>-1</sup>
$\frac{\partial Q_{\text{int}}(\theta, t)}{\partial \theta}$	Internal heating and cooling on the $\theta$ surface. Positive value denotes absorbing heat.	J s <sup>-1</sup> K <sup>-1</sup>
$\frac{\partial Q_{\text{diff}}(\theta, t)}{\partial \theta}$	Turbulent diffusive heat fluxes into the $\theta$ surface. Positive value denotes heat flux into the $\theta$ surface.	J s <sup>-1</sup> K <sup>-1</sup>

and longwave heating), dissipation of the kinetic energy of turbulence, and latent heat release due to evaporation and condensation.

To modify Eq. (A10) to apply to  $M_{\theta_e}$  rather than to  $M_\theta$ , it is necessary to replace all  $\theta$  with  $\theta_e$  and additionally account for the following:

1. Condensation and evaporation is conserved on the  $\theta_e$  surfaces, but the gaining and losing of water vapor through surface evaporation and water vapor transport contributes to  $\theta_e$ . This contribution can be computed as the product of latent heat of evaporation and the extra water vapor content. Thus, the surface contribution ( $Q_S$ ) needs to include both sensible heating of the atmosphere ( $Q_{\text{sen}}$ ) and the water vapor flux from the surface into the atmosphere ( $Q_{\text{evap}}$ ). Similarly, the diffusion term within the atmosphere ( $Q_{\text{diff}}$ ) needs to include both heat and water vapor ( $Q_{\text{H}_2\text{O}}$ ).
2. Internal heating ( $Q_{\text{int}}$ ) needs to exclude latent heat releasing due to evaporation and condensation of liquid water, which cancel in  $\theta_e$ , but it still needs to include heating from ice formation, which does not cancel in  $\theta_e$ . We subtract this ice component from the rest of the internal heating, yielding two terms  $Q'_{\text{int}}$  and  $Q_{\text{ice}}$ , with  $Q_{\text{int}} = Q'_{\text{int}} + Q_{\text{ice}}$ .

Therefore, we can write the temporal variation in  $M_{\theta_e}$  as

$$\begin{aligned} \frac{\partial}{\partial t} M_{\theta_e}(\theta_e, t) = & \int_{-\infty}^{\theta_e} \frac{\partial F_T(\theta'_e, t)}{\partial \theta'_e} d\theta'_e + \int_{-\infty}^{\theta_e} \frac{\partial F_E(\theta'_e, t)}{\partial \theta'_e} d\theta'_e \\ & - \frac{1}{C_{\text{pd}}} \left( \frac{\partial Q_{\text{diff}}(\theta_e, t)}{\partial \theta_e} + \frac{\partial Q_{\text{sen}}(\theta_e, t)}{\partial \theta_e} \right. \\ & + \frac{\partial Q_{\text{evap}}(\theta_e, t)}{\partial \theta_e} + \frac{\partial Q'_{\text{int}}(\theta_e, t)}{\partial \theta_e} \\ & \left. + \frac{\partial Q_{\text{ice}}(\theta_e, t)}{\partial \theta_e} + \frac{\partial Q_{\text{H}_2\text{O}}(\theta_e, t)}{\partial \theta_e} \right). \end{aligned} \quad (\text{A11})$$

*Code availability.* We provide R code to generate  $\theta_e$ - $M_{\theta_e}$  look-up tables from ERA-Interim meteorological fields at <https://doi.org/10.5281/zenodo.4420417> (Jin, 2021a).

*Data availability.* All HIPPO 10 s merge data are available from [https://doi.org/10.3334/CDIAC/HIPPO\\_010](https://doi.org/10.3334/CDIAC/HIPPO_010) (Wofsy et al., 2017b). Besides, all HIPPO Medusa merge data are available from [https://doi.org/10.3334/CDIAC/HIPPO\\_014](https://doi.org/10.3334/CDIAC/HIPPO_014) (Wofsy et al., 2017a). All ATom 10 s and Medusa merge data are available from <https://doi.org/10.3334/ORNDAAC/1581> (Wofsy et al., 2018).

CO<sub>2</sub> data from Mauna Loa Observatory are available from the Scripps CO<sub>2</sub> Program at [https://scrippsco2.ucsd.edu/assets/data/atmospheric/stations/in\\_situ\\_co2/monthly/monthly\\_in\\_situ\\_co2\\_mlo.csv](https://scrippsco2.ucsd.edu/assets/data/atmospheric/stations/in_situ_co2/monthly/monthly_in_situ_co2_mlo.csv) (last access: 10 July 2020; Keeling et al., 2001.). Other surface station CO<sub>2</sub> data, including Trinidad Head, Cold Bay, Barrow, Cape Kumukahi, and Sand Island, are provided by the NOAA ESRL GMD flask sampling network (<http://www.cmdl.noaa.gov/ccgg/trends>, last access: 9 July 2020) and downloaded from Observation Package (ObsPack) at <https://doi.org/10.25925/20190812> (Cooperative Global Atmospheric Data Integration Project, 2019).

The Jena CO<sub>2</sub> inversion data are available at the project website: [https://doi.org/10.17871/CarboScope-s04oc\\_v4.3](https://doi.org/10.17871/CarboScope-s04oc_v4.3) (Rödenbeck, 2005). Run ID s04oc v4.3 was used in this study.

$\theta_e$ - $M_{\theta_e}$  look-up tables with daily resolution and 1 K intervals in  $\theta_e$  from 1980 to 2018 computed from ERA-Interim are available at <https://doi.org/10.5281/zenodo.4420398> (Jin, 2021b).

*Supplement.* The supplement related to this article is available online at: <https://doi.org/10.5194/acp-21-217-2021-supplement>.

*Author contributions.* YJ carried out the data analysis and derivations. All sections in the initial draft were prepared by YJ and RFK, with critical revisions from all co-authors. BBS made important contributions to the improvement of the application part. EJM and NCP raised useful suggestions regarding the definition of  $M_{\theta_e}$ . ER provided valuable suggestions for analyzing the relationship between diabatic heating and mass fluxes.

*Competing interests.* The authors declare that they have no conflict of interest.

*Disclaimer.* Any opinions, findings, and conclusions or recommendations expressed in this material are those of the authors and do not necessarily reflect the views of the National Science Foundation.

*Acknowledgements.* The original  $M_{\theta_e}$  concept arose out of discussions during the ORCAS field campaign that included Ralph F. Keeling, Colm Sweeney, Eric Kort, Matthew Long, and Martin Hoecker-Martinez. We would like to acknowledge the efforts of the full HIPPO and ATom science teams and the pilots and crew of the NSF/NCAR GV and NASA DC-8 as well as the NCAR

and NASA project managers, field support staff, and logistics experts. In this work, we have used the HIPPO and ATom 10 s merge files, supported by the National Center for Atmospheric Research (NCAR). NCAR is sponsored by the National Science Foundation under Cooperative Agreement No. 1852977. We thank the Harvard QCLS, Harvard OMS, NOAA UCATS, and NOAA Picarro teams for sharing measurements. We thank NOAA ESRL GML for providing surface station CO<sub>2</sub> data measured at Trinidad Head, Cold Bay, Barrow, Cape Kumukahi, and Sand Island. We thank Christian Rödenbeck for sharing the Jena CO<sub>2</sub> inversion run. We thank the two anonymous reviewers for their valuable comments and efforts.

*Financial support.* This research has been supported by the National Science Foundation (grant nos. ATM-0628575, ATM-0628519, ATM-0628388, AGS-1547797, and AGS-1623748) and the NASA (grant no. NNX15AJ23G).

*Review statement.* This paper was edited by Andreas Engel and reviewed by two anonymous referees.

## References

- Arora, K., Cazenave, A., Engdahl, E. R., Kind, R., Manglik, A., Roy, S., Sain, K., and Uyeda, S.: Encyclopedia of solid earth geophysics, Springer, Dordrecht, the Netherlands, 2011.
- Bailey, A., Singh, H. K. A., and Nusbaumer, J.: Evaluating a Moist Isentropic Framework for Poleward Moisture Transport: Implications for Water Isotopes Over Antarctica, *Geophys. Res. Lett.*, 46, 7819–7827, <https://doi.org/10.1029/2019GL082965>, 2019.
- Barnes, E. A., Parazoo, N., Orbe, C., and Denning, A. S.: Isentropic transport and the seasonal cycle amplitude of CO<sub>2</sub>, *J. Geophys. Res.-Atmos.*, 121, 8106–8124, <https://doi.org/10.1002/2016JD025109>, 2016.
- Bent, J. D.: Airborne oxygen measurements over the Southern Ocean as an integrated constraint of seasonal biogeochemical processes, University of California, San Diego, USA, 2014.
- Birner, T., Do, A., and Schumann, U.: How sharp is the tropopause at midlatitudes?, *Geophys. Res. Lett.*, 29, 1–4, <https://doi.org/10.1029/2002GL015142>, 2002.
- Bolton, D.: The computation of equivalent potential temperature, *Mon. Weather Rev.*, 108, 1046–1053, [https://doi.org/10.1175/1520-0493\(1980\)108<1046:TCOEPT>2.0.CO;2](https://doi.org/10.1175/1520-0493(1980)108<1046:TCOEPT>2.0.CO;2), 1980.
- Bozem, H., Hoor, P., Kunkel, D., Köllner, F., Schneider, J., Herber, A., Schulz, H., Leitch, W. R., Aliabadi, A. A., Willis, M. D., Burkart, J., and Abbatt, J. P. D.: Characterization of transport regimes and the polar dome during Arctic spring and summer using in situ aircraft measurements, *Atmos. Chem. Phys.*, 19, 15049–15071, <https://doi.org/10.5194/acp-19-15049-2019>, 2019.
- Butchart, N. and Remsberg, E. E.: The area of the stratospheric polar vortex as a diagnostic for tracer transport on an isentropic surface, *J. Atmos. Sci.*, 43, 1319–1339, [https://doi.org/10.1175/1520-0469\(1986\)043<1319:TAOTSP>2.0.CO;2](https://doi.org/10.1175/1520-0469(1986)043<1319:TAOTSP>2.0.CO;2), 1986.

- Conway, T. J. and Tans, P. P.: Development of the CO<sub>2</sub> latitude gradient in recent decades, *Global Biogeochem. Cy.*, 13, 821–826, <https://doi.org/10.1029/1999GB900045>, 1999.
- Cooperative Global Atmospheric Data Integration Project: Multi-laboratory compilation of atmospheric carbon dioxide data for the period 1957–2018; obspack\_co2\_1\_GLOBALVIEWplus\_v5.0\_2019\_08\_12, NOAA Earth System Research Laboratory, Global Monitoring Division, <https://doi.org/10.25925/20190812>, 2019.
- Dee, D. P., Uppala, S. M., Simmons, A. J., Berrisford, P., Poli, P., Kobayashi, S., Andrae, U., Balmaseda, M. A., Balsamo, G., Bauer, P., Bechtold, P., Beljaars, A. C. M., van de Berg, L., Bidlot, J., Bormann, N., Delsol, C., Dragani, R., Fuentes, M., Geer, A. J., Haimberger, L., Healy, S. B., Hersbach, H., Hólm, E. V., Isaksen, I., Kållberg, P., Köhler, M., Matricardi, M., McNally, A. P., Monge-Sanz, B. M., Morcrette, J. J., Park, B. K., Peubey, C., de Rosnay, P., Tavolato, C., Thépaut, J. N., and Vitart, F.: The ERA-Interim reanalysis: Configuration and performance of the data assimilation system, *Q. J. Roy. Meteor. Soc.*, 137, 553–597, <https://doi.org/10.1002/qj.828>, 2011.
- Dima, I. M. and Wallace, J. M.: On the Seasonality of the Hadley Cell, *J. Atmos. Sci.*, 60, 1522–1527, [https://doi.org/10.1175/1520-0469\(2003\)060<1522:OTSOTH>2.0.CO;2](https://doi.org/10.1175/1520-0469(2003)060<1522:OTSOTH>2.0.CO;2), 2003.
- Ehhalt, D. H.: The CH<sub>4</sub> concentration over the ocean and its possible variation with latitude, *Tellus*, 30, 169–176, <https://doi.org/10.3402/tellusa.v30i2.10329>, 1978.
- Fasullo, J. T. and Trenberth, K. E.: The annual cycle of the energy budget. Part I: Global mean and land-ocean exchanges, *J. Climate*, 21, 2297–2312, <https://doi.org/10.1175/2007JCLI1935.1>, 2008.
- Foltz, G. R. and McPhaden, M. J.: The role of oceanic heat advection in the evolution of tropical North and South Atlantic SST anomalies, *J. Climate*, 19, 6122–6138, <https://doi.org/10.1175/JCLI3961.1>, 2006.
- Gelaro, R., McCarty, W., Suárez, M. J., Todling, R., Molod, A., Takacs, L., Randles, C. A., Darmenov, A., Bosilovich, M. G., Reichle, R., Wargan, K., Coy, L., Cullather, R., Draper, C., Akella, S., Buchard, V., Conaty, A., da Silva, A. M., Gu, W., Kim, G. K., Koster, R., Lucchesi, R., Merkova, D., Nielsen, J. E., Parityka, G., Pawson, S., Putman, W., Rienecker, M., Schubert, S. D., Sienkiewicz, M., and Zhao, B.: The Modern-Era Retrospective Analysis for Research and Applications, Version 2 (MERRA-2), *J. Climate*, 30, 5419–5454, <https://doi.org/10.1175/JCLI-D-16-0758.1>, 2017.
- Graven, H. D., Keeling, R. F., Piper, S. C., Patra, P. K., Stephens, B. B., Wofsy, S. C., Welp, L. R., Sweeney, C., Tans, P. P., Kelley, J. J., Daube, B. C., Kort, E. A., Santoni, G. W., and Bent, J. D.: Enhanced seasonal exchange of CO<sub>2</sub> by northern ecosystems since 1960, *Science*, 341, 1085–1089, <https://doi.org/10.1126/science.1239207>, 2013.
- Harris, J. M. and Kahl, J. D.: A descriptive atmospheric transport climatology for the Mauna Loa Observatory, using clustered trajectories, *J. Geophys. Res.-Atmos.*, 95, 13651–13667, <https://doi.org/10.1029/jd095id09p13651>, 1990.
- Harris, J. M., Tans, P. P., Dlugokencky, E. J., Masarie, K. A., Lang, P. M., Whittlestone, S., and Steele, L. P.: Variations in atmospheric methane at Mauna Loa Observatory related to long-range transport, *J. Geophys. Res.-Atmos.*, 97, 6003–6010, <https://doi.org/10.1029/92JD00158>, 1992.
- Hoskins, B. J. and Karoly, D. J.: The Steady Linear Response of a Spherical Atmosphere to Thermal and Orographic Forcing, *J. Atmos. Sci.*, 38, 1179–1196, [https://doi.org/10.1175/1520-0469\(1981\)038<1179:TSLROA>2.0.CO;2](https://doi.org/10.1175/1520-0469(1981)038<1179:TSLROA>2.0.CO;2), 1981.
- Hurst, D.: UCATS 2-Channel Gas Chromatograph (GC), Version 1.0, UCAR/NCAR Earth Observing Laboratory, Global Monitoring Division (GMD), Earth System Research Laboratory, NOAA, available at: <https://data.eol.ucar.edu/dataset/112.021> (last access: 10 May 2020), 2011.
- Jacob, D. J.: Introduction to atmospheric chemistry, Princeton University Press, New Jersey, USA, 1999.
- Jin, Y.: yumingjin0521/Mthetae Lookup Table Computation Method (Version v1.0.0), Zenodo, <https://doi.org/10.5281/zenodo.4420417>, 2021a.
- Jin, Y.:  $\theta$ -M $\theta$ e Lookup Table (ERA-Interim) (Version v1.0.0) [Dataset], Zenodo, <https://doi.org/10.5281/zenodo.4420398>, 2021b.
- Kanamitsu, M., Ebisuzaki, W., Woollen, J., Yang, S.-K., Hnilo, J. J., Fiorino, M., and Potter, G. L.: NCEP-DOE AMIP-II Reanalysis (R-2), *B. Am. Meteorol. Soc.*, 83, 1631–1643, <https://doi.org/10.1175/BAMS-83-11-1631>, 2002.
- Keeling, C. D., Piper, S. C., Bacastow, R. B., Wahlen, M., Whorf, T. P., Heimann, M., and Meijer, H. A.: Exchanges of atmospheric CO<sub>2</sub> and <sup>13</sup>CO<sub>2</sub> with the terrestrial biosphere and oceans from 1978 to 2000. I. Global aspects, SIO Reference Series, No. 01-06, Scripps Institution of Oceanography, San Diego, USA, 88 pp., 2001.
- Keppel-Aleks, G., Wennberg, P. O., and Schneider, T.: Sources of variations in total column carbon dioxide, *Atmos. Chem. Phys.*, 11, 3581–3593, <https://doi.org/10.5194/acp-11-3581-2011>, 2011.
- Li, Z. and Leighton, H. G.: Global climatologies of solar radiation budgets at the surface and in the atmosphere from 5 years of ERBE data, *J. Geophys. Res.-Atmos.*, 98, 4919–4930, <https://doi.org/10.1029/93jd00003>, 1993.
- Linz, M., Plumb, R. A., Gerber, E. P., and Sheshadri, A.: The Relationship between Age of Air and the Diabatic Circulation of the Stratosphere, *J. Atmos. Sci.*, 73, 4507–4518, <https://doi.org/10.1175/JAS-D-16-0125.1>, 2016.
- Miyazaki, K. and Iwasaki, T.: Diagnosis of Meridional Ozone Transport Based on Mass-Weighted Isentropic Zonal Means, *J. Atmos. Sci.*, 62, 1192–1208, <https://doi.org/10.1175/JAS3394.1>, 2005.
- Miyazaki, K., Patra, P. K., Takigawa, M., Iwasaki, T., and Nakazawa, T.: Global-scale transport of carbon dioxide in the troposphere, *J. Geophys. Res.-Atmos.*, 113, D15301, <https://doi.org/10.1029/2007JD009557>, 2008.
- Mooney, P. A., Mulligan, F. J., and Fealy, R.: Comparison of ERA-40, ERA-Interim and NCEP/NCAR reanalysis data with observed surface air temperatures over Ireland, *Int. J. Climatol.*, 31, 545–557, <https://doi.org/10.1002/joc.2098>, 2011.
- Parazoo, N. C., Denning, A. S., Kawa, S. R., Corbin, K. D., Lokupitiya, R. S., and Baker, I. T.: Mechanisms for synoptic variations of atmospheric CO<sub>2</sub> in North America, South America and Europe, *Atmos. Chem. Phys.*, 8, 7239–7254, <https://doi.org/10.5194/acp-8-7239-2008>, 2008.
- Parazoo, N. C., Denning, A. S., Berry, J. A., Wolf, A., Randall, D. A., Kawa, S. R., Pauluis, O., and Doney, S. C.: Moist synoptic

- transport of CO<sub>2</sub> along the mid-latitude storm track, *Geophys. Res. Lett.*, 38, L09804, <https://doi.org/10.1029/2011GL047238>, 2011.
- Parazoo, N. C., Denning, A. S., Kawa, S. R., Pawson, S., and Lokupitiya, R.: CO<sub>2</sub> flux estimation errors associated with moist atmospheric processes, *Atmos. Chem. Phys.*, 12, 6405–6416, <https://doi.org/10.5194/acp-12-6405-2012>, 2012.
- Pauluis, O., Czaja, A., and Korty, R.: The global atmospheric circulation on moist isentropes, *Science*, 321, 1075–1078, <https://doi.org/10.1126/science.1159649>, 2008.
- Pauluis, O., Czaja, A., and Korty, R.: The global atmospheric circulation in moist isentropic coordinates, *J. Climate*, 23, 3077–3093, <https://doi.org/10.1175/2009JCLI2789.1>, 2010.
- Petrovavlovskikh, I., Hoor, P., Millán, L., Jordan, A., Kunkel, D., Leblanc, T., Manney, G., and Damadeo, R.: An Overview of OCTAV-UTLS (Observed Composition Trends and Variability in the UTLS), a SPARC Activity, EGU General Assembly 2019, 7–12 April 2019, Vienna, Austria, EGU2019-12206-2, 2019.
- Prather, M. J., Flynn, C. M., Fiore, A., Correa, G., Strode, S. A., Steenrod, S. D., Murray, L. T., and Lamarque, J. F.: ATom: Simulated Data Stream for Modeling ATom-like Measurements, ORNL DAAC, Oak Ridge, Tennessee, USA, <https://doi.org/10.3334/ORNLDAAC/1597>, 2018.
- Randerson, T., Thompson, V., Conway, J., Fung, I. Y., and Field, B.: The contribution of terrestrial sources and sinks to trends in the seasonal cycle of atmospheric carbon dioxide, *Global Biogeochem. Cy.*, 11, 535–560, <https://doi.org/10.1029/97GB02268>, 1997.
- Rasmussen, R. A. and Khalil, R. A. K.: Atmospheric Methane (CH<sub>4</sub>): Trends and Seasonal Cycles, *J. Geophys. Res.*, 86, 9826–9832, <https://doi.org/10.1029/JC086iC10p09826>, 1981.
- Rödenbeck, C.: Estimating CO<sub>2</sub> sources and sinks from atmospheric mixing ratio measurements using a global inversion of atmospheric transport, Technical Report 6, Max Planck Institute for Biogeochemistry, Jena, Germany, [https://doi.org/10.17871/CarboScope-s04oc\\_v4.3](https://doi.org/10.17871/CarboScope-s04oc_v4.3), 2005.
- Rödenbeck, C., Houweling, S., Gloor, M., and Heimann, M.: CO<sub>2</sub> flux history 1982–2001 inferred from atmospheric data using a global inversion of atmospheric transport, *Atmos. Chem. Phys.*, 3, 1919–1964, <https://doi.org/10.5194/acp-3-1919-2003>, 2003.
- Santoni, G. W., Daube, B. C., Kort, E. A., Jiménez, R., Park, S., Pittman, J. V., Gottlieb, E., Xiang, B., Zahniser, M. S., Nelson, D. D., McManus, J. B., Peischl, J., Ryerson, T. B., Holloway, J. S., Andrews, A. E., Sweeney, C., Hall, B., Hints, E. J., Moore, F. L., Elkins, J. W., Hurst, D. F., Stephens, B. B., Bent, J., and Wofsy, S. C.: Evaluation of the airborne quantum cascade laser spectrometer (QCLS) measurements of the carbon and greenhouse gas suite – CO<sub>2</sub>, CH<sub>4</sub>, N<sub>2</sub>O, and CO – during the CalNex and HIPPO campaigns, *Atmos. Meas. Tech.*, 7, 1509–1526, <https://doi.org/10.5194/amt-7-1509-2014>, 2014.
- Stephens, B. B., Morgan, E. J., Bent, J. D., Keeling, R. F., Watt, A. S., Shertz, S. R., and Daube, B. C.: Airborne measurements of oxygen concentration from the surface to the lower stratosphere and pole to pole, *Atmos. Meas. Tech. Discuss.*, <https://doi.org/10.5194/amt-2020-294>, in review, 2020.
- Stull, R. B.: An introduction to boundary layer meteorology, Springer, Dordrecht, the Netherlands, 2012.
- Sweeney, C., Karion, A., Wolter, S., Newberger, T., Guenther, D., Higgs, J. A., Andrews, A. E., Lang, P. M., Neff, D., Dlugokencky, E., Miller, J. B., Montzka, S. A., Miller, B. R., Masarie, K. A., Biraud, S. C., Novelli, P. C., Crotwell, M., Crotwell, A. M., Thoning, K., and Tans, P. P.: Seasonal climatology of CO<sub>2</sub> across North America from aircraft measurements in the NOAA/ESRL Global Greenhouse Gas Reference Network, *J. Geophys. Res.-Atmos.*, 120, 5155–5190, <https://doi.org/10.1002/2014JD022591>, 2015.
- Tohjima, Y., Minejima, C., Mukai, H., MacHida, T., Yamagishi, H., and Nojiri, Y.: Analysis of seasonality and annual mean distribution of atmospheric potential oxygen (APO) in the Pacific region, *Global Biogeochem. Cy.*, 26, 1–15, <https://doi.org/10.1029/2011GB004110>, 2012.
- Tung, K. K.: On the Two-Dimensional Transport of Stratospheric Tracer Gases in Isentropic Coordinates, *J. Atmos. Sci.*, 39, 2330–2355, [https://doi.org/10.1175/1520-0469\(1982\)039<2330:OTTDTO>2.0.CO;2](https://doi.org/10.1175/1520-0469(1982)039<2330:OTTDTO>2.0.CO;2), 1982.
- Walín, G.: On the relation between sea-surface heat flow and thermal circulation in the ocean, *Tellus*, 34, 187–195, <https://doi.org/10.3402/tellusa.v34i2.10801>, 1982.
- Wang, J. W., Denning, A. S., Lu, L., Baker, I. T., Corbin, K. D., and Davis, K. J.: Observations and simulations of synoptic, regional, and local variations in atmospheric CO<sub>2</sub>, *J. Geophys. Res.-Atmos.*, 112, D04108, <https://doi.org/10.1029/2006JD007410>, 2007.
- Wexler, A.: Vapor pressure equation for water in the range 0 to 100°C, *J. Res. Natl. Bur. Stand. Sect. A Phys. Chem.*, 80A, 775–785, <https://doi.org/10.6028/jres.075a.022>, 1976.
- Wills, R. C. J. and Schneider, T.: Mechanisms setting the strength of orographic Rossby waves across a wide range of climates in a moist idealized GCM, *J. Climate*, 31, 7679–7700, <https://doi.org/10.1175/JCLI-D-17-0700.1>, 2018.
- Wofsy, S. C.: HIAPER Pole-to-Pole Observations (HIPPO): fine-grained, global-scale measurements of climatically important atmospheric gases and aerosols, *Philos. T. Roy. Soc. A Math. Phys. Eng. Sci.*, 369, 2073–2086, <https://doi.org/10.1098/rsta.2010.0313>, 2011.
- Wofsy, S., Daube, B., Jiménez, R., Kort, E., Pittman, J., Park, S., Commane, R., Xiang, B., Santoni, G., Jacob, D., Fisher, J., Pickett-Heaps, C., Wang, H., Wecht, K., Wang, Q., Stephens, B., Shertz, S., Watt, A., Romashkin, P., Campos, T., Haggerty, J., Cooper, W., Rogers, D., Beaton, S., Hendershot, R., Elkins, J., Fahey, D., Gao, R., Moore, F., Montzka, S., Schwarz, J., Perring, A., Hurst, D., Miller, B., Sweeney, C., Oltmans, S., Nance, D., Hints, E., Dutton, G., Watts, L., Spackman, J., Rosenlof, K., Ray, E., Hall, B., Zondlo, M., Diao, M., Keeling, R., Bent, J., Atlas, E., Lueb, R., and Mahoney, M. J.: HIPPO MEDUSA Flask Sample Trace Gas And Isotope Data, Version 1.0, UCAR/NCAR – Earth Observing Laboratory, [https://doi.org/10.3334/CDIAC/HIPPO\\_014](https://doi.org/10.3334/CDIAC/HIPPO_014), 2017a.
- Wofsy, S., Daube, B., Jiménez, R., Kort, E., Pittman, J., Park, S., Commane, R., Xiang, B., Santoni, G., Jacob, D., Fisher, J., Pickett-Heaps, C., Wang, H., Wecht, K., Wang, Q., Stephens, B., Shertz, S., Watt, A., Romashkin, P., Campos, T., Haggerty, J., Cooper, W., Rogers, D., Beaton, S., Hendershot, R., Elkins, J., Fahey, D., Gao, R., Moore, F., Montzka, S., Schwarz, J., Perring, A., Hurst, D., Miller, B., Sweeney, C., Oltmans, S., Nance, D., Hints, E., Dutton, G., Watts, L., Spackman, J., Rosenlof, K., Ray, E., Hall, B., Zondlo, M., Diao, M., Keeling, R., Bent, J., Atlas, E., Lueb, R., and Mahoney, M. J.: HIPPO Merged

- 10-Second Meteorology, Atmospheric Chemistry, and Aerosol Data, Version 1.0, UCAR/NCAR – Earth Observing Laboratory. [https://doi.org/10.3334/CDIAC/HIPPO\\_010](https://doi.org/10.3334/CDIAC/HIPPO_010), 2017b.
- Wofsy, S. C., Afshar, S., Allen, H. M., Apel, E., Asher, E. C., Barletta, B., Bent, J., Bian, H., Biggs, B. C., Blake, D. R., Blake, N., Bourgeois, I., Brock, C. A., Brune, W. H., Budney, J. W., Bui, T. P., Butler, A., Campuzano-Jost, P., Chang, C. S., Chin, M., Commane, R., Correa, G., Crouse, J. D., Cullis, P. D., Daube, B. C., Day, D. A., Dean-Day, J. M., Dibb, J. E., Digangi, J. P., Diskin, G. S., Dollner, M., Elkins, J. W., Erdesz, F., Fiore, A. M., Flynn, C. M., Froyd, K., Gesler, D. W., Hall, S. R., Hanisco, T. F., Hannun, R. A., Hills, A. J., Hints, E. J., Hoffman, A., Hornbrook, R. S., Huey, L. G., Hughes, S., Jimenez, J. L., Johnson, B. J., Katich, J. M., Keeling, R., Kim, M. J., Kupc, A., Lait, L. R., Lamarque, J. F., Liu, J., McKain, K., McLaughlin, R. J., Meinardi, S., Miller, D. O., Montzka, S. A., Moore, F. L., Morgan, E. J., Murphy, D. M., Murray, L. T., Nault, B. A., Neuman, J. A., Newman, P. A., Nicely, J. M., Pan, X., Paplawsky, W., Peischl, J., Prather, M. J., Price, D. J., Ray, E., Reeves, J. M., Richardson, M., Rollins, A. W., Rosenlof, K. H., Ryerson, T. B., Scheuer, E., Schill, G. P., Schroder, J. C., Schwarz, J. P., St. Clair, J. M., Steenrod, S. D., Stephens, B. B., Strode, S. A., Sweeney, C., Tanner, D., Teng, A. P., Thames, A. B., Thompson, C. R., Ullmann, K., Veres, P. R., Vizenor, N., Wagner, N. L., Watt, A., Weber, R., Weinzierl, B., Wennberg, P. O., Williamson, C. J., Wilson, J. C., Wolfe, G. M., Woods, C. T., and Zeng, L. H.: ATom: Merged Atmospheric Chemistry, Trace Gases, and Aerosols, ORNL DAAC, <https://doi.org/10.3334/ORNLDAAC/1581>, 2018.
- Yang, H., Chen, G., Tang, Q., and Hess, P.: Quantifying isentropic stratosphere-troposphere exchange of ozone, *J. Geophys. Res.-Atmos.*, 121, 3372–3387, <https://doi.org/10.1002/2015JD024180>, 2016.